BRNO UNIVERSITY OF TECHNOLOGY
VYSOKÉ UČENÍ TECHNICKÉ V BRNĚ

FACULTY OF MECHANICAL ENGINEERING
FAKULTA STROJNÍHO INŽENÝRSTVÍ

INSTITUTE OF PHYSICAL ENGINEERING
ÚSTAV FYZIKÁLNÍHO INŽENÝRSTVÍ

GROWTH OF 3D STRUCTURES INDUCED BY ELECTRON BEAM ON CERAMIC SUBSTRATES
RŮST 3D STRUKTUR NA KERAMICKÝCH SUBSTRÁTECH INDUKOVANÝ ELEKTRONOVÝM SVAZKEM

BACHELOR'S THESIS
BAKALÁŘSKÁ PRÁCE

AUTHOR — **Kristýna Bukvišová**
AUTOR PRÁCE

SUPERVISOR — **doc. Ing. David Salamon, Ph.D.**
VEDOUCÍ PRÁCE

BRNO 2017

BRNO UNIVERSITY OF TECHNOLOGY
FACULTY OF MECHANICAL ENGINEERING

Specification Bachelor's Thesis

Department:	Institute of Physical Engineering
Student:	**Kristýna Bukvišová**
Study programme:	Applied Sciences in Engineering
Study branch:	Physical Engineering and Nanotechnology
Leader:	**doc. Ing. David Salamon, Ph.D.**
Academic year:	2016/17

Pursuant to Act no. 111/1998 concerning universities and the BUT study and examination rules, you have been assigned the following topic by the institute director Bachelor's Thesis:

Growth of 3D Structures Induced by Electron Beam on Ceramic Substrates

Concise characteristic of the task:

Observation by Scanning Electron Microscopy (SEM) may cause structural changes of the observed object. Such changes are sometimes called contamination, however conditions for formation of 3D objects are so far not satisfactory described. Suitable substrate for investigation of surface changes induced by electron beam are ceramics materials. These materials have high thermal stability and high chemical resistance. Materials selected for this project are based on zirconia and titania with various microstructures. Determination of critical conditions necessary for formation of 3D structures is crucial for fundamental understanding of physical and chemical processes induced by electron beam in SEM environment.

Goals Bachelor's Thesis:

1. Describe possibilities of formation electron beam induced 3D structures – literature review.
2. Experimentally evaluate formation of 3D structures induced by electron beam in environment of scanning electron microscope. Substrates selected for testing are ceramic materials based on zirconium oxide or titanium oxide.

List of literature:

Utke, I., Hoffmann, P., Melngailis, J., Gas-assisted focused electron beam and ion beam processing and fabrication, J Vac Sci Technol B 26(4) (2008) 1197-1276.

Postek, M. T., Vladar, A. E., Purushotham, K. P., Does Your SEM Really Tell the Truth? Part 2, Scanning Microscopies 2013: Advanced Microscopy Technologies for Defense, Homeland Security, Forensic, Life, Environmental, and Industrial Sciences 8729 (2013).

Lee, S. W., Sankaran, R.M., Direct writing via electron-driven reactions, Mater Today 16(4) (2013) 117-122.

Deadline for submission Bachelor's Thesis is given by the Schedule of the Academic year 2016/17

In Brno,

L. S.

prof. RNDr. Tomáš Šikola, CSc. Director of the Institute	doc. Ing. Jaroslav Katolický, Ph.D. FME dean

Abstrakt
Vystaví-li se vzorek působení elektronového svazku, dojde na jeho povrchu ke strukturním změnám. Jednou z těchto změn je vertikální růst 3D struktur na keramických materiálech. V práci jsou zkoumány podmínky nutné pro takový proces. Nárůst teploty často zapříčiní povrchové změny, proto je v práci proveden výpočet ohřevu materiálu elektronovým svazkem.
Dále je zkoumán vliv různých parametrů svazku na růst 3D struktur, závislost objemu a rozměrů je analyzována pomocí AFM.
Výsledný odhad nárůstu teploty se pohybuje v řádech jednotek, maximálně desítek K. Výrazný objemový růst je pozorován pro nízká urychlovací napětí a malé proudy. Výška vzniklých struktur dosahuje 100 nm za minutu a je nepřímo úměrná velikosti proudu.

Klíčová slova
Rastrovací elektronová mikroskopie, kontaminace, tepelné účinky elektronového svazku, oxidové keramiky.

Summary
Irradiation of a sample surface by the electron beam is known to cause structural changes. One type of these changes is vertical growth of 3D structures on surface of ceramic materials. In the thesis, the conditions necessary for such processes are analysed. A calculation of heating effect of the electron beam is conducted, since a temperature rise can trigger several surface changes. Impact of various e-beam parameters on the growth of 3D structures is investigated. Changes of volume and dimensions of the structures related to the beam parameters are studied using the AFM.
The estimated temperature increase is in range of units or maximally tens of K. Significant volumetric growth rate is observed at low voltages and currents. Height of the grown structures can reach 100 nm per minute and depends inversely on beam current.

Keywords
Scanning electron microscopy, contamination, electron beam heating, ceramic oxides.

BUKVIŠOVÁ, K. *Growth of 3D Structures Induced by Electron Beam on Ceramic Substrates*. Brno: Brno University of Technology, Faculty of Mechanical Engineering, 2017. 51 s. Supervisor doc. Ing. David Salamon, Ph.D.

I declare that I have written this thesis on my own, under the supervision of my bachelor's thesis supervisor. I have used no other resources, except those cited and mentioned in references.

Brno Kristýna Bukvišová

I wish to express my gratitude to my supervisor, doc. Ing. David Salamon, Ph.D., for his valuable guidance, encouragement and comments to the thesis' drafts. I owe my thanks to Ing. Jakub Zlámal, Ph.D. for his extensive help with the temperature calculations and Juraj Bobek for helping me with AFM measurement. SIMS analysis was conducted by Radek Holeňák and Ing. Petr Bábor, Ph.D. so I would like to thank them, too. I am also grateful to my family and friends for their support during my studies.

This work was carried out with the support of CEITEC Nano Research Infrastructure (ID LM2015041, MEYS CR, 2016–2019), CEITEC Brno University of Technology.

Kristýna Bukvišová

Contents

1. Introduction

Electron beam exposition in an electron microscope is known to alter the surface of the observed sample. Changes of the structure and vertical growth of 3D structures have been observed on surfaces of ceramic materials. Conditions necessary for the process and the observed mass transfer have not been quantitatively described yet. The main objective of this thesis is to analyse these changes for titania and zirconia ceramic materials.

The first part of this thesis (chapter 2) generally describes the processes taking place upon electron beam exposition and theoretical foundations of electron beam – specimen interaction simulations.

Non-conductive materials are known to be problematic to observe in a scanning electron microscope (SEM) due to unwanted charging and possible heating damage. Monte Carlo simulations of electron penetration through the sample combined with heat transfer calculations can give an approximation of the possible temperature rise upon electron beam irradiation. An elevated temperature causes increase of surface mobility and that generates good conditions for superficial structures growth. Methods used to determine the temperature rise are described in section 3.1.

Another hypothesis considered is that it is a deposition of hydrocarbons which causes the growth. Contamination is a commonly observed fact, but not so easily described since surface diffusion is relatively complex. In section 2.5.4, there is a simplified summary of the processes causing it and a documented rate dependence on various factors.

Section 3.2 includes an attempt to quantify the observed processes. The method and arisen problems are described there, as well. The structures are fabricated in two different scanning electron microscopes and some of them are analysed by atomic force microscopy. The investigated beam parameters are especially beam current, spot size and accelerating voltage. Kinetics of the growth are analysed by comparing structures manufactured for different irradiation times.

In section 4.3, first results of composition analysis of the grown 3D structures are presented.

2. Theoretical foundation

2.1. Ceramic oxides

Ceramic oxides are currently the most produced group of ceramic materials. The term "advanced ceramics" stands mostly for oxides of metals such as aluminium, zirconium, titanium and rare earth elements. Their preparation demands raw materials of high quality and purity and the processing conditions must be carefully controlled. In the recent past, methods of fabrication ceramics of various properties have been extensively studied, especially chemical inertness, hardness, optical, electrical and magnetic properties [1].

This work concentrates on processes taking place at the surface of titanium dioxide and yttria-stabilized zirconium dioxide.

Zirconium dioxide (ZrO_2 or zirconia) is an oxide with high melting temperature (2880 °C) and a very low thermal conductivity. It is characterized by its strength, toughness and chemical stability.

It exists in three polymorphs: tetragonal, cubic and monoclinic. Transformation from monoclinic to tetragonal zirconia is associated with a decrease in volume (approximately 3–5 %).

Pure zirconia becomes monoclinical below 1170 °C and to produce sintered pieces, it must be combined with other oxides – stabilizers. These are usually MgO, CaO and Y_2O_3.

Because of its low thermal conductivity, zirconia often serves as a thermal barrier. It can also be used for manufacturing ionic conductors. The stabilizers cause an increased concentration of interstitials and vacancies. The residual oxygen atoms show an increased mobility and stabilized zirconia offers properties of ionic conductors, hence, their application as solid electrolytes and sensors [2, 3].

Titanium dioxide (TiO_2 or titania) has unusual properties, such as thermal and chemical stability, semi-conducting properties, photo-catalytic activity and biocompatibility. It exists in the following crystalline modifications: anatase (tetragonal), rutile (tetragonal) and brookite (rhombohedral). Their unit cells are shown in Figure 2.1. Other structures can be prepared, for example cotunnite – one of the hardest polycrystalline materials.

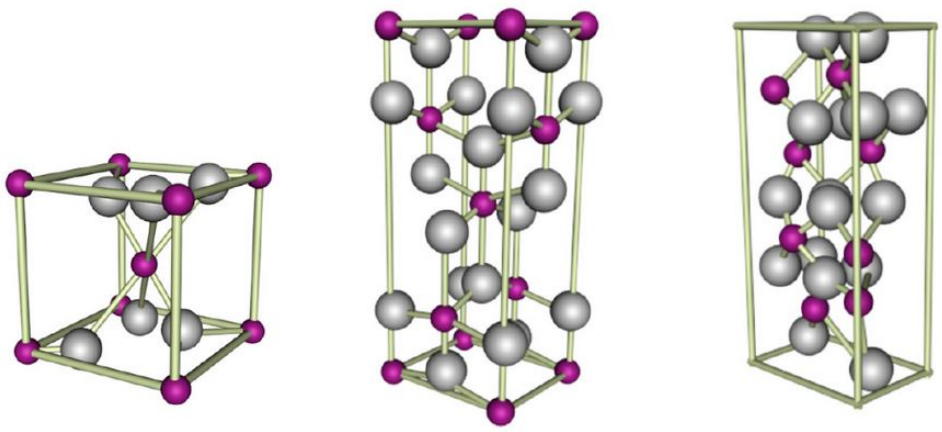

Figure 2.1: Unit cells of rutile, anatase and brookite respectively, adapted from [5].

Rutile and anatase have good pigmentary properties. Rutile is more thermally stable than anatase, both anatase and brookite irreversibly transform to rutile above approxi-

mately 800 °C. The phase transformation has been extensively studied and it was proved that it depends significantly on defect concentration, grain boundary concentration and particle packing [1, 4].

It can be chemically reduced above approximately 900 °C which has a great effect on conductivity. Oxygen loss can lead to formation of nonstochiometric (Magneli) phases and Ti_2O_3, Ti_3O_4 and TiO [5, 6].

Polycrystalline titania is a functional ceramic material interesting especially for its electric properties which are highly influenced by trace elements, impurities and processing factors.

2.2. Scanning electron microscope

The scanning electron microscope (SEM) is a widely used instrument to study topography and other properties on micro and nanoscale because the spatial resolution is much better than that of optical microscopes since it uses high-energy electron beam to generate signals at the surface of solid samples. The earliest SEM was designed in Germany in 30's and the first commercial version in 1965.

A simple schematic showing the principle of the scanning electron microscope is shown in Figure 2.2.

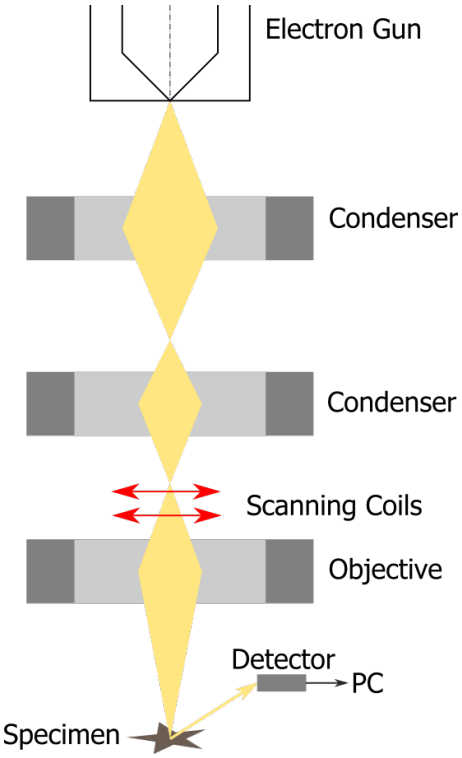

Figure 2.2: A simplified schematic of SEM. Electrons are produced in an electron gun and accelerated to a selected voltage. As the beam passes through two condenser lenses, it is focused. Various apertures limit the effects of aberrations. The scanning coils deflect the beam in xy plane and the scan produces a desired signal collected by a detector. Based on a figure from [7].

The electron source in SEM can be a tungsten filament, LaB_6 or Schottky emitter. Tungsten filaments emit electrons due to their heating – a small number of the electrons

have a sufficient thermal energy to escape the wire. This process is called thermionic emission. The emission current density can be expressed as the Richardson law:

$$J_e = AT^2 \exp(-\Phi/k_{\mathrm{B}}T), \tag{2.1}$$

where T is the temperature in K, A is the Richardson constant ($\approx 10^6\,\mathrm{A{\cdot}m^{-2}{\cdot}K^{-2}}$), k_{B} is the Boltzmann constant and kT represents the mean thermal energy of a conduction electron near Fermi level. LaB_6 is an improved cathode – it is very stable and has a low work function which improves the emission current. It needs a better vacuum ($< 10^{-4}$ Pa) in order not to become poisoned due to reaction with residual oxygen. The thermionic emission can be improved by applying an electrostatic field to the filament surface. It lowers the height of the potential barrier which the electrons need to overcome in order to leave the cathode.

The electrons leaving the source are accelerated by a strong electric field. The range of accelerating voltages used is usually 0,1–30 kV. Its choice influences the image quality and strength of different signals as well as the effect on the specimen. Commonly, the emission of secondary electrons (SE) is used for obtaining the image but sometimes it is more preferable to use the backscattered electrons (BSE).

The secondary electrons are atomic electrons which escape the specimen as a result of inelastic scattering. Most SE are generated with an energy below 100 eV. Since the probability of inelastic scattering depends inversely on kinetic energy, the electrons lose their energy very quickly. The result is that SE which escape the sample are generated within a very small depth below the surface ($< 2\,\mathrm{nm}$). This dimension is referred to as the escape depth. The SE signal therefore represents the surface structure (topography). The angle between the incident beam and the sample surface is a great factor for the signal strength – the higher the specimen tilt (the angle between the surface normal and the beam), the higher the SE yield.

The backscattered electrons are incident electrons which undergo multiple elastic scattering and are ejected back from the specimen surface. Their energy is not much smaller than the incident energy and they can therefore escape the sample from considerably bigger depths than SE. Imaging using BSE is different from SE imaging in two ways. The depth from which the detected electrons originate is up to about half of the penetration depth. The other difference is that the signal offers chemical contrast since the BSE yield increases with atomic number of the specimen [8]. A more detailed view of the processes taking place upon e-beam irradiation is given in section 2.3.

2.3. Electron beam-specimen interaction

To understand the reason for changes at the thick specimen surface, it is important to consider how incident electrons interact with it. The electrons undergo two types of scattering: inelastic and elastic. For inelastic scattering, a part of the incident electron energy is lost due to interactions with the orbital electrons of the specimen atoms. There are many possible effects: generation of secondary electrons (SE), backscattered electrons (BSE), heating, X-ray radiation (characteristic, continuum), visible light photons and Auger electrons, which only achieve to leave the sample when generated near the surface. Most of the lost energy is therefore converted to heat. Figure 2.3 shows the signals generated by the electron beam.

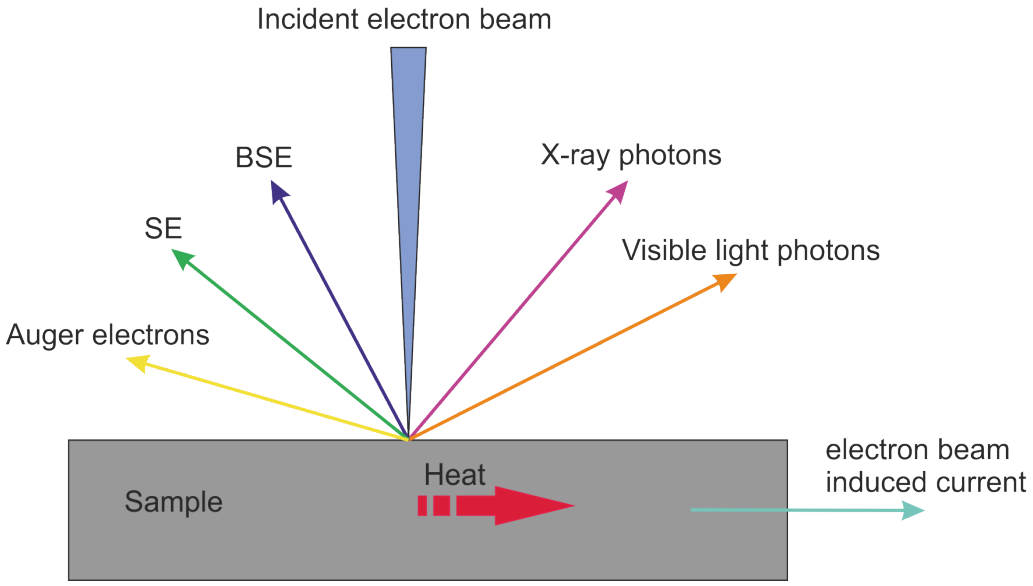

Figure 2.3: Signals generated by electron beam irradiation. Based on [7].

If the transferred energy is converted into momentum, atomic displacements can be created. This happens if the transferred energy exceeds displacement energy E_d, which is dependent on the specimen material. In some cases, the scattering can displace atomic nuclei to interstitial positions and degrade the original crystalline structure. Most of the energy of the electrons which undergo inelastic scattering is lost to heating the sample. Sputtering can also occur when the electron transfers sufficient energy to a surface atom but that process is unlikely for low voltage microscopy. For transmission electron microscopy which operates with voltages in ranges of hundreds of kV, sputtering is a common problem [9].

If an incident electron transfers a part of its kinetic energy to a weakly bound valence or conduction electron, a small part of this energy is used up for releasing the particle from a nucleus potential and the rest is converted to kinetic energy. The escaped electrons travel in the sample as secondary electrons [8]. For very low accelerating voltages, the incident electrons can have smaller energies than energy levels in atoms, so the number of inelastic scattering events decreases. If the incident energy is sufficiently high, the probability of inelastic scattering depends inversely on the energy.

If the electron undergoes elastic scattering, its trajectory changes but energy is lowered minimally. Some electrons can be backscattered from the sample in case of multiple elastic scattering and can be used for imaging (BSE). Probability of elastic scattering increases with atomic number of the specimen. The atomic number contrast is strong, the cross section for high angle scattering is proportional to Z^2 [8, 10].

The region which the beam penetrates is known as the interaction volume. Its shape and size depends on many factors, such as beam parameters (intensity, high voltage, beam angle) and atomic number of the specimen material. There are direct methods to visualize the interaction volume for low atomic number materials (etching plastics, for example polymethylmethacrylate), for materials with high atomic number, there is an indirect method – Monte Carlo electron trajectory simulation. This approach has a limited validity – the trajectories are calculated independently and so there is no consideration of mutual influence of a field generated by a large number of electrons in the real beam in case of high current densities.

2.4. Influence of the specimen composition on the interaction volume

The interaction volume is a function of specimen tilt, composition and beam properties. In cross section, it has a pear-like shape [8]. With increasing landing energies, the interaction volume and the depth of penetration increases since it takes more scattering events for electrons to lose most of their kinetic energy. The shape of the interaction volume is however relatively independent on the beam energy.

The atomic number of the sample material influences both the shape and the size of the interaction volume. In specimens of high atomic number, the electrons are more frequently elastically scattered and the average angle at which they are scattered is bigger as well, which means that electrons deviate from their original directions more quickly. This dependence is shown in Figure 2.4.

The angle formed by incident beam and the flat sample surface determines the asymmetry of the interaction volume, the higher the angle, the smaller the interaction volume.

The shape for a specific set of beam properties and a material must be determined by Monte Carlo simulations.

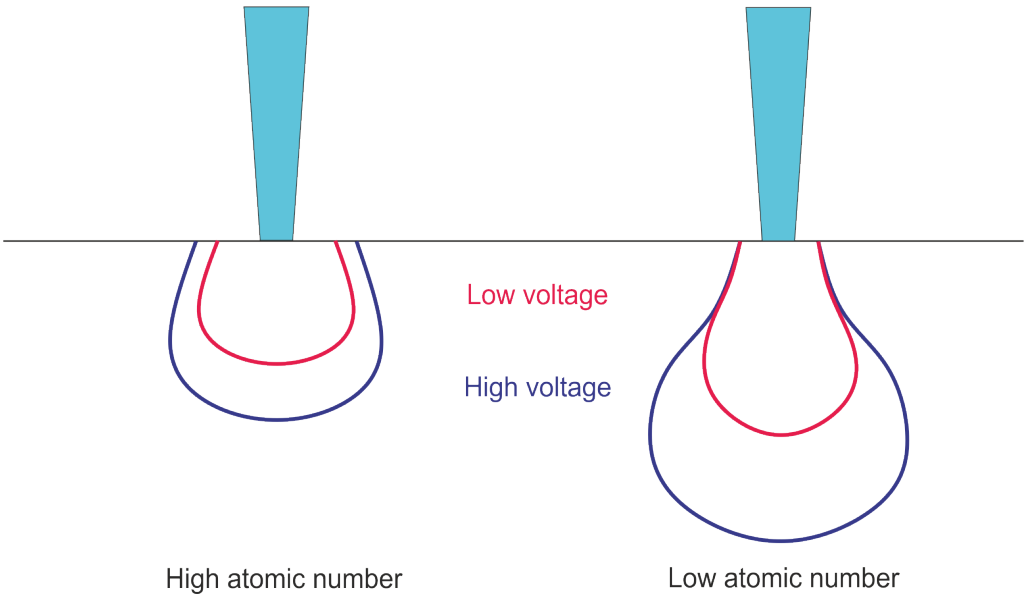

Figure 2.4: Comparison of interaction volumes for different samples and incident beam energy. Based on [8].

Analytic expressions offer a less accurate description of ranges of interaction and distribution, but they say a lot about the influence of sample composition and incident energy. For lower energies (below 10 kV), the maximum range of the electron penetration can be estimated as

$$R = 900\rho^{-0,8}E_0^{1,3}, \tag{2.2}$$

where R is in Å, ρ in g/cm^3 and E_0 in keV. For higher accelerating voltages, the dependence differs [11].

The density of absorbed energy E_a of beam in matter in eV/cm^3 can be described by formula

$$E_a = \frac{Q \cdot E_0}{e \cdot R_g}\lambda(f), \tag{2.3}$$

where Q is the exposition dose in C/cm^2, E_0 is the accelerating voltage in eV, R_g is Grün range (the depth of penetration) in cm, e is the elementary charge in C and $\lambda(f)$ is a cubic polynomial expressing the ratio of depth and dose using the normalized depth $f = z/R_g$:

$$\lambda(f) = 0{,}74 + 4{,}7f - 8{,}9f^2 + 3{,}5f^3. \tag{2.4}$$

The values of absorbed density are higher for lower incident energies due to lower R_g [12].

2.5. Radiation damage in low voltage SEM

Upon electron beam irradiation, many temporary and permanent changes in sample surface structure can come to pass. This chapter contains an overview of different types of this damage dominant for low voltage SEM (< 5 kV) [9].

2.5.1. Electron beam heating

Inelastic scattering involves interaction between incident electrons and atomic electrons and this process can involve a significant energy transfer. Most of this energy is converted to heat, eventually.

For good thermal conductors and high accelerating voltages, the consequential temperature rise is negligible. Beam heating is known to be a problem for high incident currents and low conductive samples ($0{,}2{-}2\,\mathrm{W{\cdot}m^{-1}{\cdot}K^{-1}}$), such as polymers.

According to [9], in SEM, an approximation for the temperature increase ΔT in a bulk specimen is

$$\Delta T = \frac{1{,}5}{\pi}\frac{IV_0}{\kappa R}, \tag{2.5}$$

where I is the probe current, V_0 the accelerating voltage, κ is the thermal conductivity and R is the characteristic electron range. Using this approximation, data for yttria-stabilized zirconia in table 3.1 and $I = 150\,\mathrm{pA}$, $V_0 = 2\,\mathrm{kV}$, $R = 40\,\mathrm{nm}$, we can obtain a temperature increase $\Delta T = 3{,}8\,\mathrm{K}$.

It is also known that for lower voltages ($500\,\mathrm{V}{-}2\,\mathrm{kV}$), thin films or organic specimens in SEM can be heated to a few hundred degrees for a stationary probe.

2.5.2. Electrostatic charging

When there is not a balance of electrons received by a specimen and those which leave it, it becomes electrically charged. As a result, an electric field worsening the conditions for collecting electrons is generated. The incident beam can be deflected and it can become impossible to get an image in SEM. Wise choice of the accelerating voltage is therefore necessary. The current balance for a conductive sample can be described by the following equation:

$$I_\mathrm{B} = (\delta + \eta)I_\mathrm{B} + I_\mathrm{SC}, \tag{2.6}$$

where I_B is the incident beam current, δ is SE yield, η BSE yield and I_{SC} is the current flowing between the specimen and ground. In case the sample is non-conductive, I_{SC} is close to zero and the rate of charge build-up ΔQ per second can be expressed as

$$\frac{\Delta Q}{\Delta t} = I_B(1 - (\delta + \eta)). \tag{2.7}$$

At specific ranges of voltages, $\delta + \eta$ is either greater or lower than 1. Especially at low voltages, $\delta + \eta$ is greater than 1 and the specimen therefore becomes positively charged.

Positively charged areas re-collect its secondary electrons and therefore appear dark in the SE image. Negatively charged regions look bright, as the detector collection efficiency is increased (secondary electrons are repelled from the surface and their landing energy is lowered, hence greater SE yield).

There are two beam energies E_1 and E_2, for which an equilibrium ($\delta + \eta = 1$) is achieved. E_1 is typically in ranges from 50 to 150 eV and E_2 is between 0,5 and 3 keV. For energies E, where $E_1 < E < E_2$, the surface charges positively [13].

2.5.3. Radiolysis

Two most common mechanisms of specimen damage are knock-on damage and radiolysis. Knock-on damage (removal of surface atoms) happens if the incident electron energy exceeds atomic sputtering threshold energy. Radiolytic damage stands for atomic displacement induced as a result of momentum transfer between incident electrons and atoms of the sample. The majority of damage in low voltage microscopy is radiolytic [10].

2.5.4. Hydrocarbon layer formation

Electron-beam-induced specimen contamination is a problem of every SEM. In vacuum, the mobility of carbon residues is higher than in air and all clean surfaces are quickly covered by adsorbed organic molecules. Upon electron beam irradiation, the hydrocarbon molecules can be broken and a thin layer of polymerized hydrocarbons can cover the surface of the exposed sample. Formation of the layer is influenced by many factors, especially e-beam energy, current and temperature of the sample.

When the concentration of adsorbed molecules in the area exposed to the electron beam decreases, as there is a new cross-linked layer, more molecules diffuse to it. This process results in a continuous growth of contamination. This becomes more apparent in case of a stationary beam.

The rate of contamination increases with lower electron energy proportionally to the Bethe stopping power, which approximates energy loss of electrons due to inelastic scattering (ionisation). Low landing energy electrons generate more SE leaving the sample, which cause more dissociation of organic molecules which then easily form the unwanted hydrocarbon layer.

Common deposition rates are a few tens of nanometres per second but in instruments with better vacuum, the rate is smaller. High accelerating voltages mask the hydrocarbon layer to an extent because the beam easily penetrates low atomic number surface as long as it is thin enough.

For higher current densities, the organic vapours polymerize faster, but the rate is limited by the presence of free surface hydrocarbons. Especially for currents below 100 pA, the

amount of contamination increases with higher beam current and longer dwell times [14]. According to different sources, however, the contamination rate increases monotonously with $1/I$ [15].

With increasing temperature, the rate of contamination increases as well because the surface mobility of atoms is a key factor causing the continuous hydrocarbon layer formation. Lower temperatures do not prevent it entirely but the rate is significantly reduced.

The shape of contamination layers depends on the beam spot size and the method of scanning. For a stationary beam, the structure is a single peak, whereas a crown-like shape is common for larger irradiated areas or spot size (Figure 2.5).

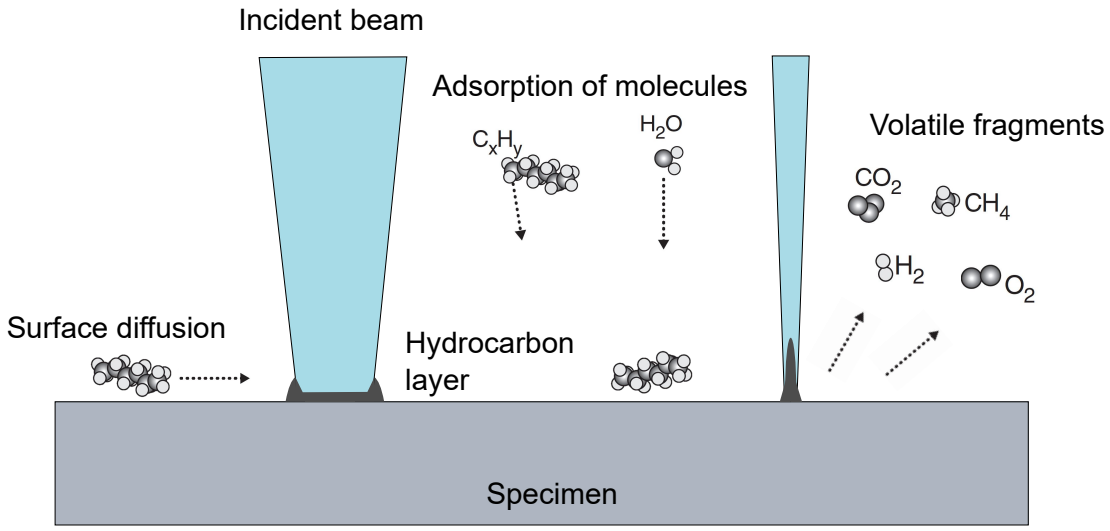

Figure 2.5: The common shapes of formed contamination for a wide and a narrow beam. A similar dependence is valid when considering the size of the irradiated area. Figure based on [16].

Description of processes taking place in hydrocarbon layer formation is rather complicated – surface mechanisms are complex and the conditions are unique for each measurement and the identity of the residual hydrocarbon dominant in deposition reaction is hard to predict [17].

A relatively simple view of the mechanism was suggested by Müller [15].

The Hertz–Knudsen formula describes the incident flux of molecules F.

$$F = \frac{p}{(2\pi m k_{\mathrm{B}} T)^{1/2}}, \tag{2.8}$$

where p is the partial pressure of organic molecules, m is molecular mass, k_{B} is the Boltzmann constant and T is temperature.

The constant τ_0 describes the time between the adsorption and the following desorption of the molecules. Therefore, the resulting change of concentration of adsorbed molecules n per time can be estimated as

$$\left(\frac{\partial n}{\partial t}\right)_1 = -\frac{n}{\tau_0}. \tag{2.9}$$

Local changes in the concentration $n(\vec{r})$ result in a flux $j_n = -D\nabla n$, where D is the diffusion constant.

$$\left(\frac{\partial n}{\partial t}\right)_2 = D\nabla^2 n. \tag{2.10}$$

The beam damages the adsorbed layer of molecules with a cross section σ_d, a cross section σ_c describes the decrease in concentration n caused by its polymerization. The combined cross section $\sigma = \sigma_d + \sigma_c$ describes the change in concentration due to these processes together, their rate can be, hence, expressed as

$$\left(\frac{\partial n}{\partial t}\right)_3 = -\frac{\sigma j}{e} n, \tag{2.11}$$

where j is the current density and e is the elementary charge.

When all the contributions are combined together, we obtain the following partial differential equation

$$\frac{\partial n}{\partial t} = F - \frac{n}{\tau_0} + D\nabla^2 n - \frac{\sigma j}{e} n. \tag{2.12}$$

Solving the equation is simplified when a cylindrical symmetry is considered.

After obtaining $n(\vec{r})$, the hydrocarbon layer thickness x_c can be calculated from

$$x_c(\vec{r}, t) = \overline{m}\frac{\sigma_c j}{e} \int_{t_0}^{t} n(\vec{r}, t')dt', \tag{2.13}$$

where $\overline{m}$ is the mean mass of cross linked molecules.

The main downside of this description is that it does not include the effect of an induced electric field at the surface. The molecules migrate in a different way than without its presence and it can be a very important factor especially for non-conductive samples and a stationary probe. It describes quite well the hydrocarbon layer formation for conductive samples irradiated in a larger area in a scanning mode (short dwell times) [15]. Solution of the previous problem is corresponding to the experimental results – a crown-like shape of the hydrocarbon layer, the biggest contamination is at the periphery of the irradiated area. Typical sample contamination is in Figure 2.6.

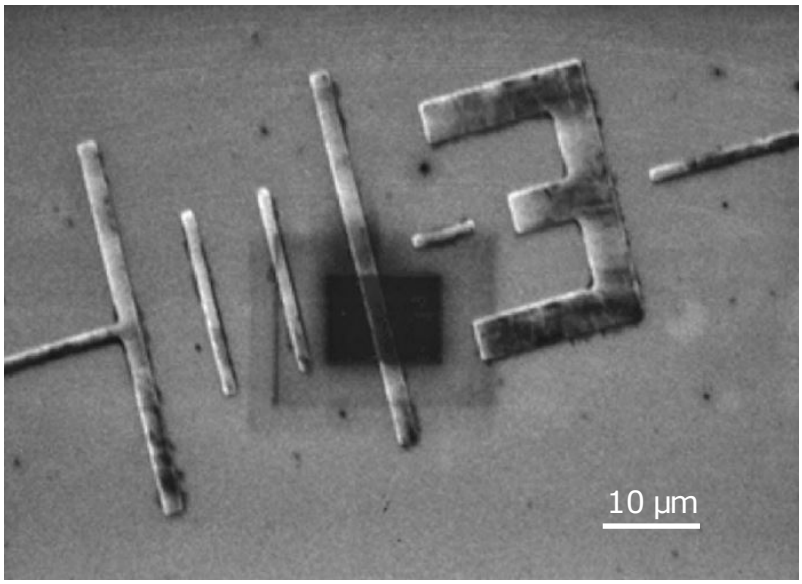

Figure 2.6: A contamination observed on the surface of a patterned silicon wafer sample. Adapted from [18].

In study [17], surface transport equation (STE) is solved for a stationary beam. Since the secondary electrons have an energy corresponding to peak dissociation cross section

energies, they are the major contributors to hydrocarbon decomposition. Simulation of SE generation combined with solving STE provides a description of dynamic growth of a nanopillar (for a stationary electron beam). The electron energies considered in this study are in range 5−30 keV. Three regimes of nanostructure generation are identified: reaction limited, diffusion limited and mixed. In the first case, the surface diffusion is much faster than the deposition reaction, as opposed to the diffusion limited case, in which the surface diffusion is slower. Height at the centre of the nanopillar increases with time linearly for reaction-limited regime. The volumetric growth according to $1 - e^{-t}$ is obtained for diffusion limited process. The vertical growth rate is calculated to be in units or tens of nm per second.

A presence of water adsorbed on a surface can have a dramatic effect on the contamination. In fact, a presence of residual water can cause hydrocarbon layer etching. The electron-dissociated water is known to be able to destroy carbon-based samples. It can react with the polymerized hydrocarbons and produce volatile products. Deposition of hydrocarbon layers and their etching therefore happen simultaneously during electron beam irradiation in high-vacuum chambers [16].

2.6. Effect of e-beam on ceramic oxides

It is known that the surface of TiO_2 crystals is reduced during annealing at high temperature in vacuum. The electron radiation damage can cause reduction to TiO or even metallic Ti. There have been studies of these changes induced by transmission electron microscope (TEM) and the morphological changes are explained by generation of metallic Ti by reduction and increase in their mobility due to the temperature rise. Under specific conditions, there is an equilibrium established between the surface reduction and re-oxidation. Many factors can influence this equilibrium and a presence of other elements can adjust the preference of one process. Another possible explanation considered in the study is vapor transport of Ti atoms by e-beam sputtering. There are many studies of nanostructure formation induced by TEM and usually the substrate is a thin layer of TiO_2 anatase [19]. Surface diffusion of excess Ti atoms plays a key role in the formation of these nanostructures as well as the oxygen pressure.

Surface oxygen can be removed as a consequence of ion sputtering and the surface can have a high concentration on Ti cations. As a result, the surface can be reoxidized, while the bulk undergoes reduction. Charge and mass is transported between the surface and the bulk, likely through the diffusion of point defects (oxygen vacancies or interstitial titanium). Using secondary ion mass spectroscopy, such processes can be observed and described [20].

There have been many studies on electron stimulated desorption (ESD) inducing oxygen desorption in TiO_2 (110). ESD was demonstrated for high beam currents, 10−50 A/cm^2, as well as lower currents, 1,2 $\mu A/cm^2$. In study [21], such defects are described for relatively low electron beam energies (0,48 and 1 keV) and low current densities ($\mu A/cm^2$). Under these conditions, surface Ti^{3+} defects were generated. The effects were similar to those produced by thermal annealing or ion sputtering. The rate of defect formation was greater for 0.48 keV than 1 keV.

Similar processes are documented for yttria-stabilized zirconia as well [22].

2.7. Calculations of electron trajectories and energy loss in solids

Electron beam lithography (EBL) is a commonly method used for nanofabrication. In order to adjust the lithographic processes, it is useful to look closely at the beam–sample interaction characteristics. An accessible way of determining the properties of interaction volume and the amount of energy transferred to the sample is a simulation of electron movement through the sample.

Total cross section describes the probability of scattering event and the probability of a specific angle between the incident and scattering direction of the particle is determined by the differential inelastic scattering cross section $\mathrm{d}\sigma/\mathrm{d}\Omega$ which is a function of the scattering angle θ. Trajectories for a large number of electrons must be calculated to get a statistical significance.

The movement of electrons through a sample is calculated by multiple electron scattering. The Monte Carlo method is used for simulating the individual random scattering events. The basic approach is based on the Rutherford elastic scattering differential cross section (DCS) and continuous slow down approximation (CSDA) with the Bethe stopping power for determining energy loss through the sample.

The simplest differential cross section formula is the Rutherford scattering cross section

$$\frac{\mathrm{d}\sigma}{\mathrm{d}\Omega} = \frac{e^4 Z^2}{4\left(4\pi\epsilon_0\right)^2 E^2}\left(\frac{E + m_0c^2}{E + 2m_0c^2}\right)^2 \frac{1}{\left(1-\cos\theta\right)^2}, \tag{2.14}$$

where Z is the atomic number, ϵ_0 is vacuum permittivity, e, m_0 and E are the electron charge, mass and energy, respectively; θ is the scattering angle and c is the speed of light.

The stopping power [keV/cm] is often calculated using Bethe approximation

$$\frac{\mathrm{d}E}{\mathrm{d}s} = -\frac{7,85\cdot 10^4 \rho}{E}\frac{Z}{A}\ln\left(\frac{1,166E}{J}\right), \tag{2.15}$$

where the J is the mean ionization potential in eV, ρ is the sample density, A is atomic weight and E is the electron energy in eV. The mean ionization potential represents an average over several shells.

There are limitations, more sophisticated DCS and CSDA models must be used to simulate the interaction with materials composed of atoms of high atomic number, thin films or for the case of a low incident beam energy [16, 23]. One of these approaches is for example Mott DSC, which takes into consideration relativistic effects and is particulary relevant for calculations at low incident energies [10]. It is relatively complex but analytical approximations of the total Mott cross section are available. It is a function of primary electron energy, atomic number, scattering angle and complex empirical models. Figure 2.7 shows a difference between Rutherford and Mott DCS for gold and two different electron energies.

Simulation programs are accessible and frequently used to determine the parameters for electron-beam lithography processes – one of them is CASINO. It employs the continuous slowing down approximation to calculate the energy absorbed by the specimen and Mott cross sections (and other models) to estimate the trajectories and scattering of electrons. The stopping power is based on Bethe approximation with an improved formula for the mean ionization potential by Joy and Luo [16].

The situation gets more complex with porous samples and more complex 3D structures.

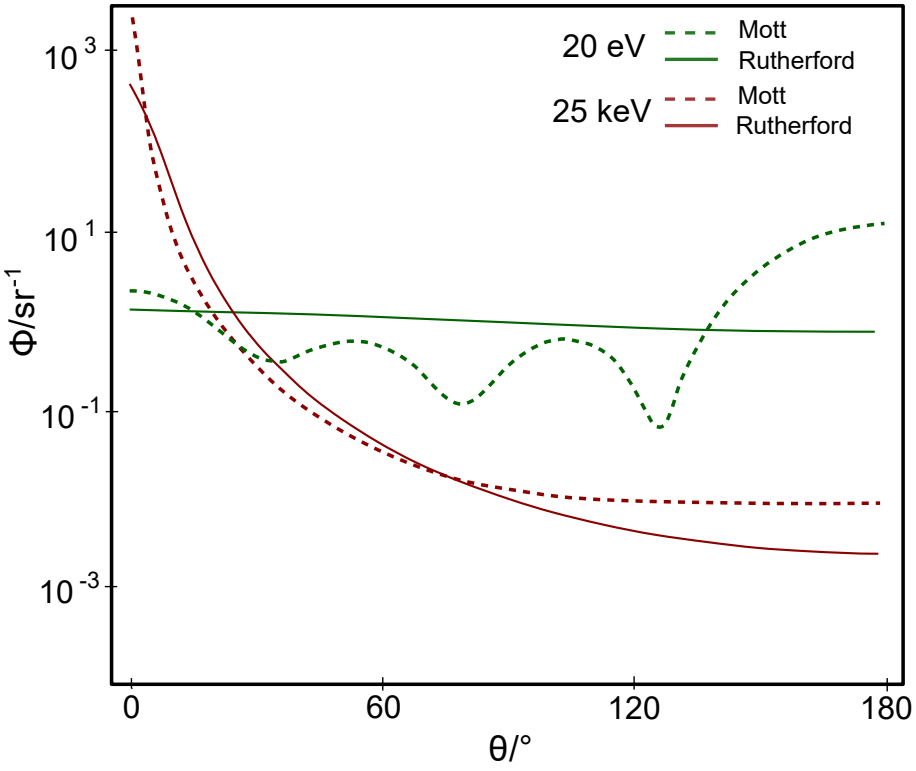

Figure 2.7: Differential scattering cross sections for Rutherford and Mott models. For very low energies, the two differ substantially. Figure based on [31].

2.8. Atomic force microscopy

One of the most convenient ways of analysing surface topography is using atomic force microscope (AFM). This method was first presented in 1986 by G. Binnig, C. F. Quate and Ch. Gerber in Zurich [24]. The main advantage of AFM is the ability to scan non-conductive samples and its high precision. Very small images can be collected to measure the crystallographic structure of samples. A simple schematic diagram is shown in Figure 2.8. In the basic setup, the sharp tip (ideally ending with only one atom) interacts with the sample. The force influences the the position of the cantilever, which deflects the laser beam. This change is recorded by a position-sensitive photodiode. Segmented quadrant sensors are used when performing both vertical and horizontal analysis.

The potential which describes the interaction between two neutral atoms is the Lennard-Jones potential

$$V_{LJ} = 4\epsilon \left[\left(\frac{\sigma}{r}\right)^{12} - \left(\frac{\sigma}{r}\right)^{6} \right], \tag{2.16}$$

where σ is the distance between the atoms at which the potential is zero, r is the distance between the atoms and ϵ is the potential well depth.

There are three imaging modes: contact, tapping and non-contact. In contact mode, the tip is pressed onto the surface by a constant force or is at a constant height. It operates in the interval of repulsive interaction. Its downside can be a possible damage to the sample and the tip but it is relatively fast. Tapping and non-contact modes are dynamic, which means that the cantilever oscillates at the resonant frequency (or slightly

above it) and it operates in the area of attractive interaction. Changes in frequency, phase and amplitude can be monitored and different forms of feedback can follow depending on the measurement specification.

The tapping mode is probably the most commonly used one since it combines the advantages of both – it conserves the lateral resolution but eliminates the lateral friction which causes problems for contact mode [25].

More information about AFM and its modifications can be found in [25].

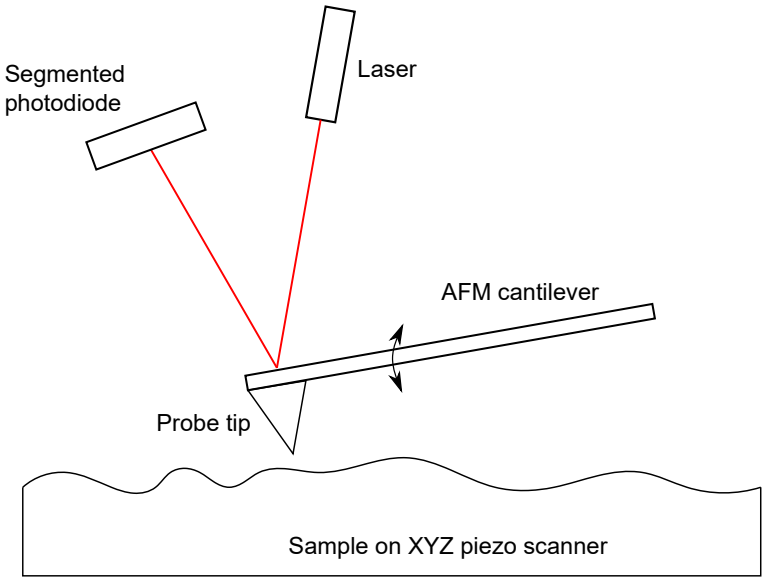

Figure 2.8: A schematic diagram showing the principle of AFM. The deflection of the laser beam determines the differences of signal between the segments of the photodiode and therefore maps the topography of the sample.

3. Methods

3.1. Calculation of electron beam induced temperature rise

Many processes taking place upon electron beam irradiation show an increased rate with higher temperatures. Determining the temperature rise could shed some light on the mechanisms of the observed structures growth. There are not many possible ways to do so – direct measurement is fairly complicated because of the fact that the irradiated area has a size of tens of nanometres.

The following calculations are meant to offer an estimation of the thermal effects. Choosing physical models for Monte Carlo electron trajectory and energy transfer simulation and the applied boundary conditions in heat transfer calculations are the very influential. One of the uncertain parameters is the beam spot size. All of these factors are discussed in this chapter and explanations for the specific choices or approximations are given.

3.1.1. Simulations in CASINO v2.42

CASINO (Monte Carlo Simulation of Electron Trajectory in Solids) is a software developed especially for modelling low-energy beam interactions in bulk and thin samples. A guide for using the program was article [26].

The main goal was to get a 3D energy loss map which could be used as an input for heat transfer calculations.

Electron energy loss and the consequential temperature rise were calculated for TiO_2 and 3Y-TZP (3 molar percent yttria stabilized zirconia) substrates. The program uses user defined densities (Table 3.1) and weight fractions of elements. Since 3Y-TZP contains only a small fraction of yttria and it would be problematic to define in the software, the sample's composition was considered as pure zirconia. The error is not significant, other factors influence the result much more.

Table 3.1: Properties used for the calculations [27, 28].

	TiO_2 (rutile)	3Y-TZP
density	$4{,}23\,\mathrm{g{\cdot}cm^{-3}}$	$6{,}05\,\mathrm{g{\cdot}cm^{-3}}$
thermal conductivity	$7{,}4\,\mathrm{W{\cdot}m^{-1}{\cdot}K^{-1}}$	$2{,}0\,\mathrm{W{\cdot}m^{-1}{\cdot}K^{-1}}$
heat capacity	$690\,\mathrm{J{\cdot}kg^{-1}{\cdot}K^{-1}}$	$400\,\mathrm{J{\cdot}kg^{-1}{\cdot}K^{-1}}$

One of the encountered issues was determining the beam radius. In the calculations, the spot size used was calculated by TESCAN software Real time In-Flight Beam Tracing™. The second used microscope (FEG SEM Zeiss Ultra Plus) only provides information about the pixel size, but the actual spot size is not given.

The real spot size depends on the focus and as ceramic materials tend to be difficult to observe, the ideal calculated spot size is always smaller than the real one.

Selection of the models for electron – mass interaction and energy loss is very influential. Cross sections calculated by Mott are particularly relevant for low energy calculations [10], so they were chosen for the simulation.

After that, the program can export data of energy absorbed per unit volume in keV divided by the number of electrons. These values were modified to be a compatible input for COMSOL Multiphysics. An example of the graphic representation of the output data for 3Y-TZP is presented in Figures 3.1 and 3.2.

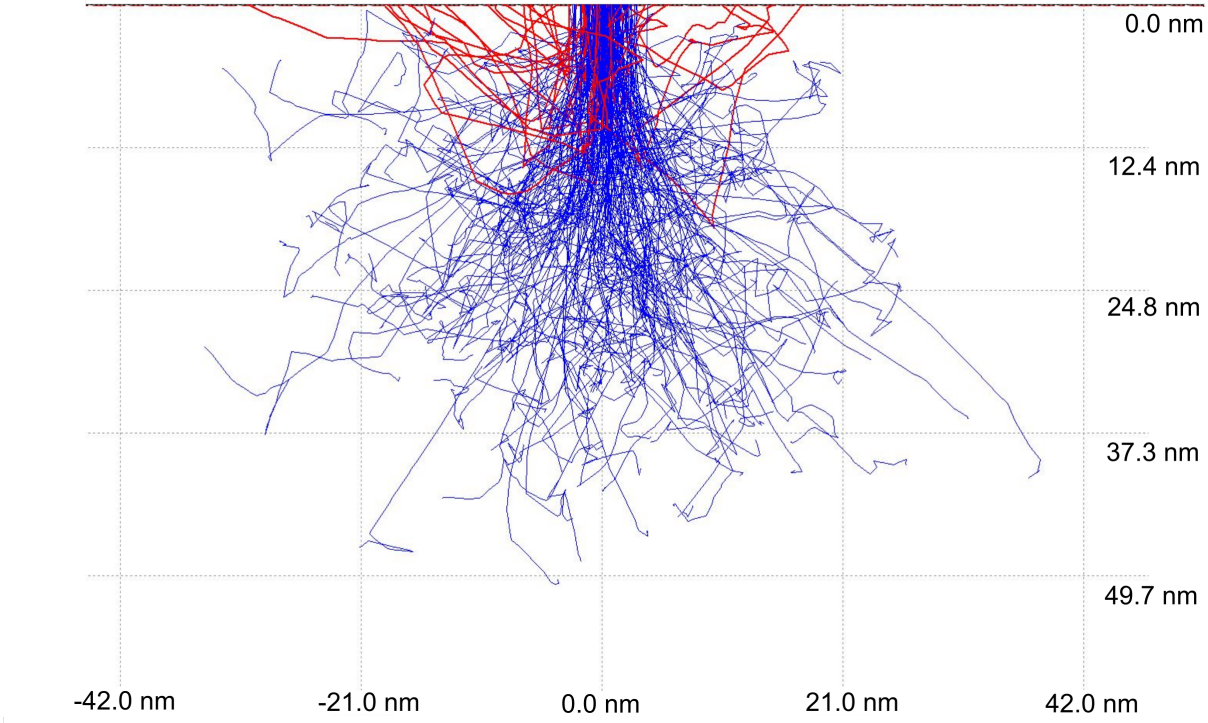

Figure 3.1: Visualisation of electron trajectories in titania for 2 kV accelerating voltage, spot size 8 nm. Red lines represent electrons which escape from the sample.

Table 3.2 shows penetration depths for various voltages, which were useful for choosing dimensions of the domains for the following calculations in COMSOL.

Table 3.2: Penetration depths for various accelerating voltages.

accelerating voltage/kV	penetration depth/nm TiO_2	ZrO_2
0,5	6,2	5,5
1,0	15,1	13,5
1,5	26,2	22,7
2,0	38,6	31,8
2,5	54,3	44,5
3,0	70,6	56,1
4,0	112,2	79,5
5,0	152,9	120,0

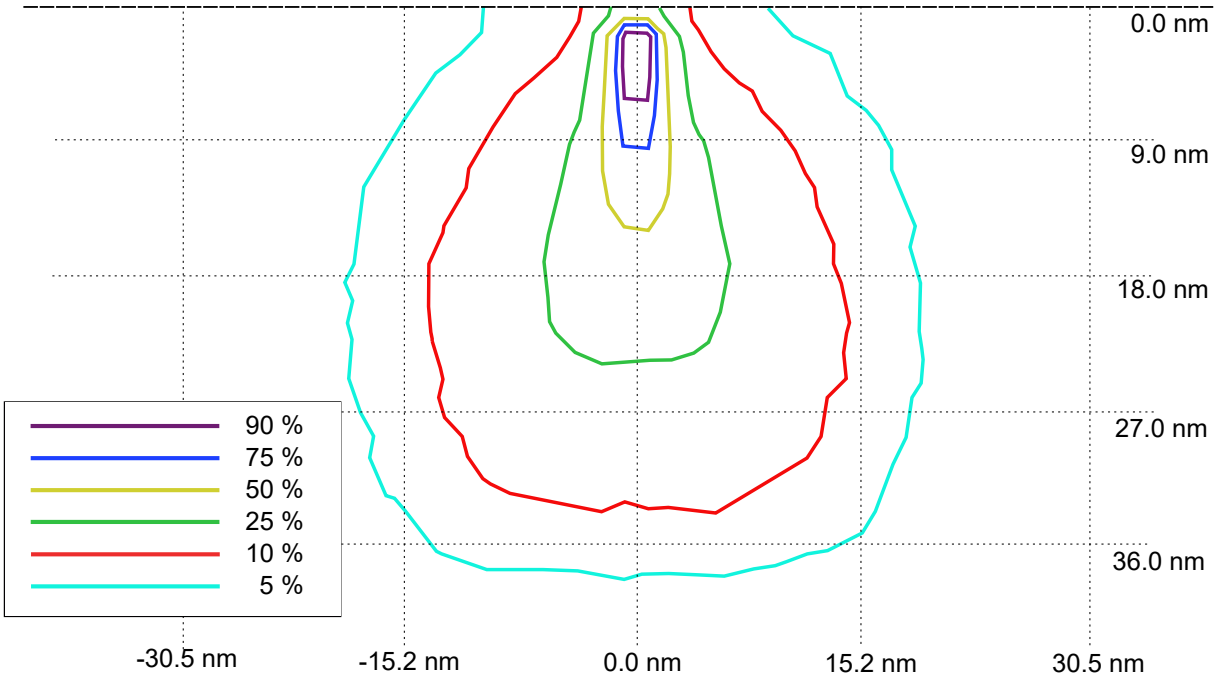

Figure 3.2: Visualisation of the absorbed energy in titania for parameters: accelerating voltage 2 kV, spot size 8 nm. The energy contour lines show the energy not contained within the volume defined by the lines. Number of electrons whose trajectories were calculated is 10^5.

3.1.2. Calculation of heating in COMSOL Multiphysics®

COMSOL Multiphysics® is a software using finite element analysis to solve problems described by differential equations. Using the Heat Transfer Module, the heat transfer equation was solved and the temperature rise in the sample was determined.

The model definition and boundary conditions

Three main areas are defined in the model and because the problem has a cylindrical symmetry, the areas are cylinders of three sizes. The smallest one in the center (A1) has the most dense mesh, the largest one (A3) the least dense and the middle one (A3) serves as the transitional area (the mesh density lowers further from the smallest central cylinder as shown in Figure 3.3). The dimensions are chosen so that the size of the largest cylinder is very large compared to the beam penetration radius and depth. Their dimensions are shown in Table 3.3. Area A1 contains all of the absorbed beam energy and is expected to show the most significant temperature changes, the mesh is therefore most dense.

Table 3.3: Dimensions of the domains.

Domain	Radius	Height
A1	40 nm	150 nm
A2	120 nm	225 nm
A3	25 µm	40 µm

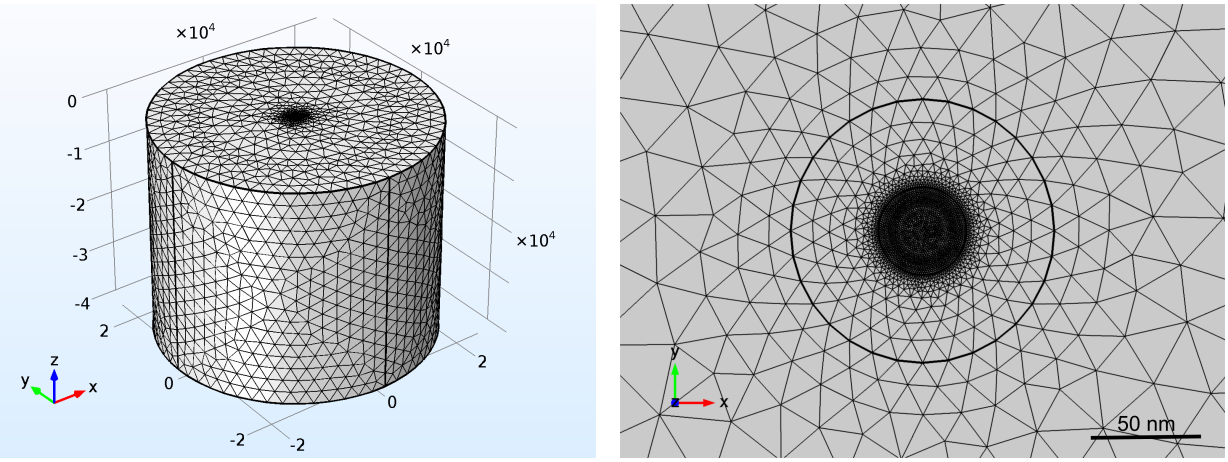

Figure 3.3: Left: The mesh in 3D, the scale is in nm. Right: Top view of the mesh. The areas' borders are displayed as thicker lines.

The equation, which is to be solved, is the heat equation

$$\rho C_p \frac{\partial T}{\partial t} - \nabla \left(k \nabla T \right) = Q, \tag{3.1}$$

where ρ is the solid density, C_p is the heat capacity at constant pressure, k is the conductivity and Q is the heat source. Properties calculated with are in Table 3.1 and Q is a combination of surface radiation and energy provided by the beam.

The boundary conditions are schematically displayed in Figure 3.4. The lateral area is considered thermally insulated, which means that $\vec{n} \cdot (k \nabla T) = 0$. This condition was chosen since the temperature is not likely to change significantly so far from the heat source. The base in contact with the surrounding is radiating. Emissivity of the surface was chosen to be 0,9. No specific value for the used oxide ceramics was found so this parameter was estimated as a typical value found for alumina (Al_2O_3) [29].

The initial temperature of the large cylinder was set as 293,15 K as well as the ambient temperature.

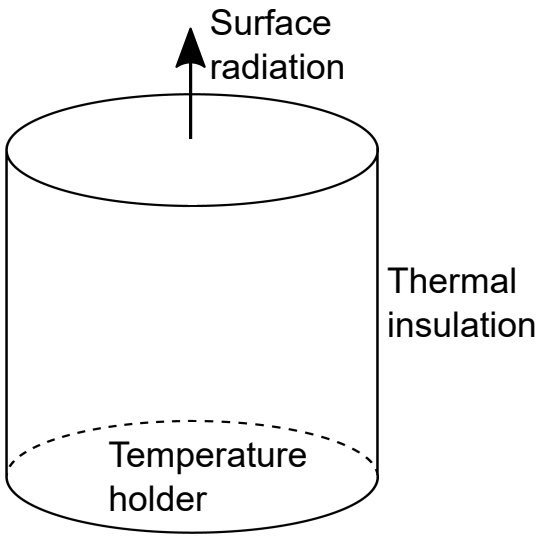

Figure 3.4: A schematic view of the boundary conditions.

Heat source parameters and arising limitations

From the data provided by CASINO software, total amount of energy which an average electron transfers to the sample was calculated. For beam accelerating voltage 2,0 kV, the result was approximately 1,5 keV per electron.

Two approaches were considered: the easier one was solving the stationary heat equation at the cost of losing information about temperature dependence on time. This approach is commonly used for estimating the temperature rise due to beam irradiation (it corresponds with equation 2.5). The stationary problem can show us the maximum temperature within the cylinder, under such conditions, the beam power is equal to the heat loss (especially due to radiation). The biggest problem of this approach is especially the fact that the electrons enter the material individually and their relaxation times are very short compared to the time between two electron impacts.

For example, let the accelerating voltage be 2 kV and the current of incident electrons $I = 150\,\mathrm{pA}$. Average time t_b between electrons can be estimated as

$$t_b = \frac{\mathrm{e}}{I} = \frac{1,602 \cdot 10^{-19}\ \mathrm{C}}{150 \cdot 10^{-12}\ \mathrm{A}} = 1,07\,\mathrm{ns}. \tag{3.2}$$

When compared with the time it takes for the electron to scatter in the sample (relaxation or thermalization time), time t_b is relatively long. Common electron relaxation times for electrons of 10 kV are 10^{-14} s. This result can be obtained for previously discussed conditions using the formula [30]

$$\tau = \frac{E_0^2}{3\pi N Z \mathrm{e}^4 v_0}, \tag{3.3}$$

where E_0 is the incident electron kinetic energy, N is the number of atoms per unit volume, Z is the atomic number, e is the elementary charge and v_0 is the velocity of the electron with energy E_0. The formula is derived by considering the time needed for the electron to lose its energy, which is described by the Bethe stopping power 2.15.

One way of adjusting the model and calculations is distributing the heating power of the beam so that it corresponds to individual pulses of transferred energy. Another question must be asked: is it even possible to speak about temperature rise due to a single electron scattering event? The power increase is significant and much higher temperatures can be calculated, but the nature of temperature is statistical and the standard description of thermal transport on macro scale has its limitations. Another important consideration involves the lattice relaxation times which are much longer than 10^{-14} s. As to the power distribution calculated, it is obtained by averaging energy loss along the trajectory of a large number of electrons.

Based on [31], calculating the heat transfer using the Fourier thermal transport equation (3.1) for a large amount of electrons gives relatively accurate results. Since only a rough estimation of temperature increase is desired, the basic stationary approach should suffice. In order to obtain a more accurate solution, a two-temperature model would have to be used. It considers temperatures of phonons and electrons and their equilibrium but is considerably more complex and requires more sophisticated methods.

3.2. Growth of 3D structures

Longer observation of ceramic oxides has been known to sometimes trigger growth of material. These morphological changes could just be contamination. However, only certain observation conditions caused this effect. In this work, testing different materials, beam parameters and comparing the process in two different SEMs was conducted – Tescan LYRA3 and FEG SEM Zeiss Ultra Plus. LYRA is better for lithographic uses whereas Zeiss SEM has a better imaging ability (even for very low currents, the spot and therefore pixel size are much smaller). The grown structures were analyzed by AFM Nenovision Litescope^{TM}.

3.2.1. Sample preparation

TiO_2 samples were prepared from titania nanopowder (Aeroxide P25, primary particle size 21 nm) by Spark plasma sintering method[1], which allows rapid densification within minutes and grain growth can be suppressed [32]. Sintering conditions were:

- c-sample: heating rate 100 °C/min to 900 °C, dwell time 2 min, mechanical pressure 50 MPa was applied at 700 °C
- d-sample: heating rate 100 °C/min to 1000 °C, dwell time 2 min, mechanical pressure 50 MPa was applied at 700 °C.

3Y-ZrO_2 samples were prepared from tetragonal zirconia with 3 molar percent Y_2O_3 (3Y-TZP), the average green particle size was 80 nm (grade TZ-3Y, Tosoh Co., Japan) by sintering in high temperature furnace. Before the sintering process, the powder was formed into green bodies by compacting it with uniaxial pressing at 25 MPa followed by cold isostatic pressing (CIP) at 300 MPa. By this procedure the disk-shaped green bodies (weight about 6 g, diameter ca 15 mm, thickness 6,2−7,0 mm depending on the powder compaction) were fabricated. Organic compounds being present in the powder "as received" were burnt out in air at 600 °C for one hour. Pressure-less sintering conditions were 100 °C/min to 1500 °C, dwell time 2 min.

Both types of samples were cut to half and polished down to roughness 1 μm. Afterwards, thermal etching was applied at 1300 °C for 10 minutes to show the microstructure.

3.2.2. Experimental setup

Observing non-conductive ceramic materials in an electron microscope always presents a great number of obstacles. The beam voltage must be carefully chosen, usually the limit for a comfortable image formation without an excessive charging is 5 kV. The emission current is a similarly important factor – there must be a balance found since a low intensity can help omit the excessive charge build-up but, at the same time, the SE signal must be strong enough to obtain a decent image.

The following procedure was conducted using LYRA3. The chamber was cleaned with a plasma decontaminator prior to the measurement at 50 Pa for 10 minutes. At first, the same procedure as that for electron lithography was used – areas of various shapes

[1] sintering by DC current which allows the heating and cooling rate to be very high

and defined electron dose were irradiated using DrawBeam[2]. The alternate approach was drawing dots and lines with known dwell times. This approach saves a lot of time but it is also reported to increase the contamination rate. It enabled the manufacturing of a large number of dot arrays and lines and deducing how the parameters influence the growth rate and shapes of the objects.

A lot of e-beam parameters were considered in order to quantify the structures' growth, especially the current density (and as it turns out, the current itself), accelerating voltage and the beam dwell time.

3.2.3. Analysis of the grown structures

In the SEM, determining the shape and size of very small objects can be challenging. The sample can be tilted or different signals (SE, BSE) can be compared. One of the most accessible methods of surface topography characterization is AFM – the topography was studied in Nenovision Litescope™. Since the structures are sometimes difficult to find, the combination of SEM and AFM was ideal. Litescope™ proved to be a fast way of verification and quantification of the growth.

Akiyama Probe was used for imaging, its specification is in Table 3.4. AFM used in this work does not need a laser to measure deflection, since the probe is connected to a piezo tuning fork.

Table 3.4: Akiyama Probes specifications [34].

Cantilever	length: 310 µm, thickness: 3,7 µm, width: 30 µm, n-type, highly doped silicon
Tip	tip radius: < 15 nm, tip height: 28 µm
Force constant	5 N/m
Resonance frequency	40−60 kHz

Dimensions and the shape of structures were analysed in Gwyddion v2.47. Height of the structures was measured as a difference between maximal height and the background. The background value was taken as an average in the vicinity of the individual structures and the error was estimated from the roughness around them. The confidence selected was 95% and the data distribution was assumed to be normal. Spot size calculated with when estimating current densities was taken from data provided by TESCAN software Real time In-Flight Beam Tracing™.

The figures in section 4.2 were obtained by comparing the heights for structures created relatively close from one another (approx. 1−2 µm). Based on experience, the results differ a bit as the sample ages.

[2]DrawBeam is a software for advanced patterning in SEM and FIB-SEM lithographic applications. It allows the electron or ion exposition or ion milling of various patterns [33].

4. Results

4.1. Results of the calculations

Table 4.1 summarizes the results for both materials. The beam parameters were chosen to represent typical values for our experiment. The temperatures are the maximal values of temperature rise along the axis of symmetry. These maxima were achieved just below the surface (less than 10 nm).

Table 4.1: The results for beam spot size 8 nm, current 150 pA and various accelerating voltages.

	ΔT/°C	
V/kV	Zirconia	Titania
0,5	1,7	0,5
1	1,9	0,6
1,5	1,7	0,5
2	1,6	0,4
3	1,4	0,3

The temperature rise along the axis of symmetry for zirconia is shown Figure 4.1.

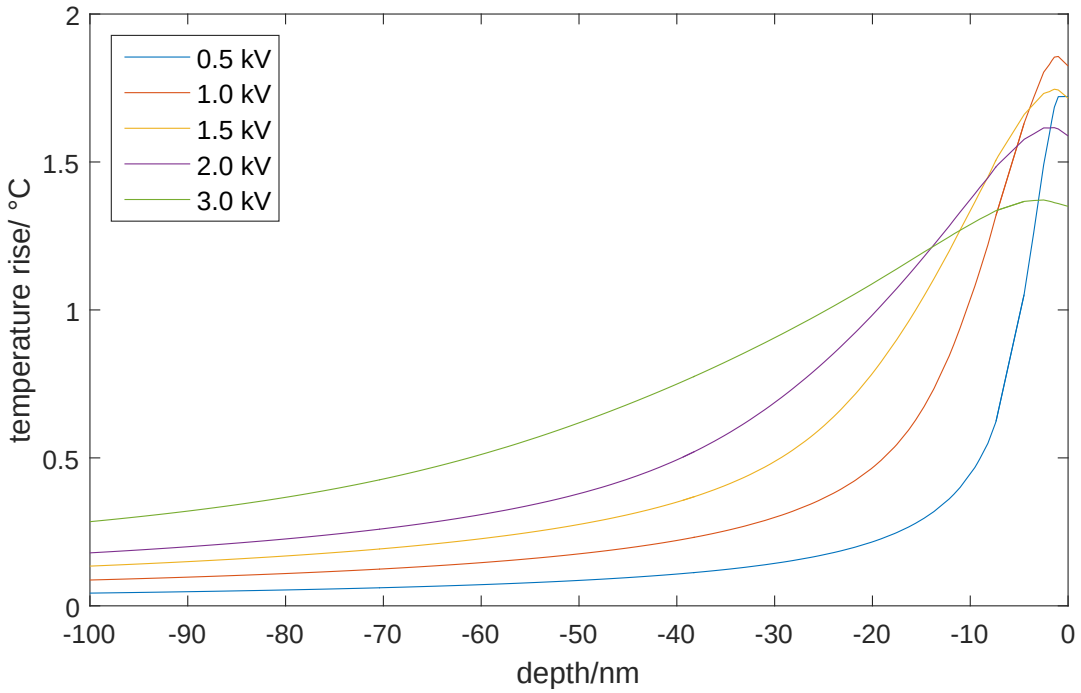

Figure 4.1: Temperature rise profile along the axis of symmetry in zirconia. For accelerating voltage 1 kV, local rise is highest.

The result is straightforward – there is no reason to assume that the material is heated in a substantial way and the possibility of thermally driven crystalline changes can be dismissed.

Beam current for 2 kV accelerating voltage and spot size 8 nm, which would induce a temperature rise above 1000 °C in titania, was calculated. It would have to be a little below 100 nA. Since the growth was observed for both materials and the currents were substantially lower than 100 nA, heating on this scale is impossible.

If the electron heating was to be considered as pulses, one pulse lasting 10^{-11} s would (according to the presented model) induce maximum heating in titania shown in Figure 4.2. The time of the pulse is much longer than calculated according to equation 3.3 because of the lattice relaxation times.

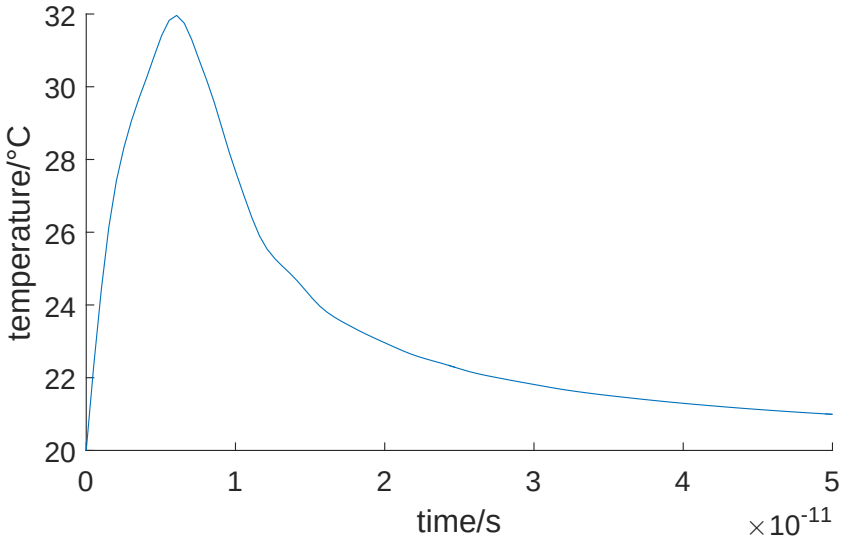

Figure 4.2: Theoretical maximum temperature for a 10^{-11} s pulse of heat. It indicates that the temperature decreases substantially before the next electron penetrates the sample. It is unlikely that this approach would give results much different from the stationary model. The only difference is that for a short time, the temperature is higher than originally computed.

4.1.1. Experimental verification of the calculation

To determine the validity of the results and the model, PLA (polylactic acid) was irradiated for 60 s at various beam intensities. Then, the effect on the surface was observed. The first changes caused by heating should be present when heated up to 50 °C (glass transition temperature). The parameters are in Table 4.2.

According to the calculations, the temperature increased only by 5 °C for beam current 63 pA. For this current, however, some surface change was present. It was most likely only a result of radiation damage rather than heating since the surface looked a little shrunk.

Table 4.2: Parameters of polylactic acid [35].

Composition	Density	Heat capacity	Thermal conductivity
$C_3O_2H_4$	1,3 g·cm^{-3}	1800 J·kg^{-1} ·K^{-1}	0,13 W·m^{-1}·K^{-1}

4.2. Observed growth

Irradiating large areas with a specified dose and dwell time per pixel had very few results. The outcome was a rather random growth but no specific beam settings were found to trigger the structural changes. A commonly observed effect was a drift of the beam due to the excessive charging. This made it impossible to irradiate larger surfaces with a desired electron dose. An example of the growth achieved by this method can be seen in Figure 4.3. Irradiating single points provided more control of the electron dose.

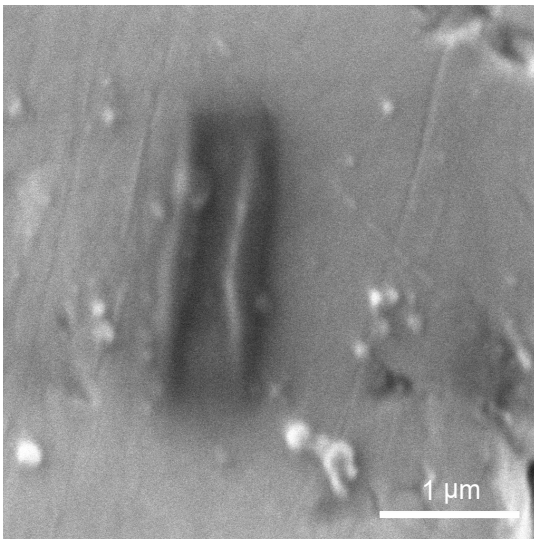

Figure 4.3: SEM image (LYRA3) showing an example of badly chosen conditions - voltage 2 kV, current 368 pA, dose 3 mC/cm^2, (intended) irradiated area 0,5×0,5 µm. Substrate: zirconia.

Figure 4.4 shows examples of a dot array and a line successfully grown in FEG SEM Zeiss.

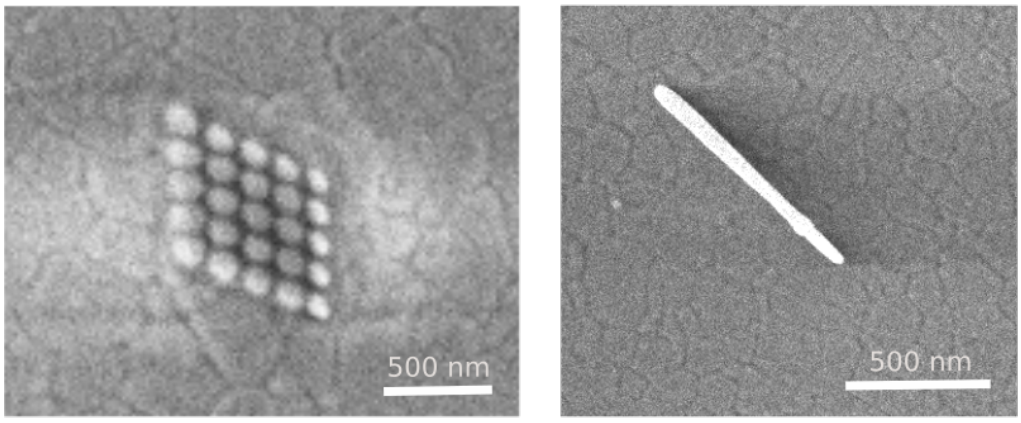

Figure 4.4: SEM image (FEG SEM Zeiss) of successfully grown structures. Substrate: zirconia.

An example of the topography profiles obtained by AFM measurement used for determining the following dependencies is shown in Figure 4.5.

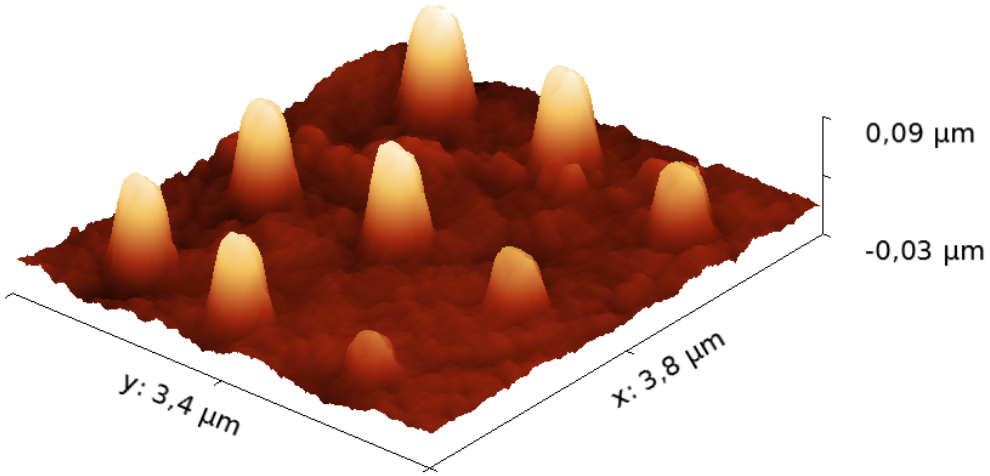

Figure 4.5: AFM image (Nenovision Litescope) of the grown structures showing height dependence on dwell time. Accelerating voltage 2 kV, beam current 12 pA, dwell times 10−90 s, substrate TiO_2 c.

4.2.1. Height dependence on beam dwell time

Figure 4.6 shows the height dependence for different irradiation times. Table 4.3 shows an estimation of other parameters.

Table 4.3: Table of beam settings.

Accelerating voltage	Current	Spot size	Current density
2 kV	103 pA	11 nm	108 A·cm^{-2}

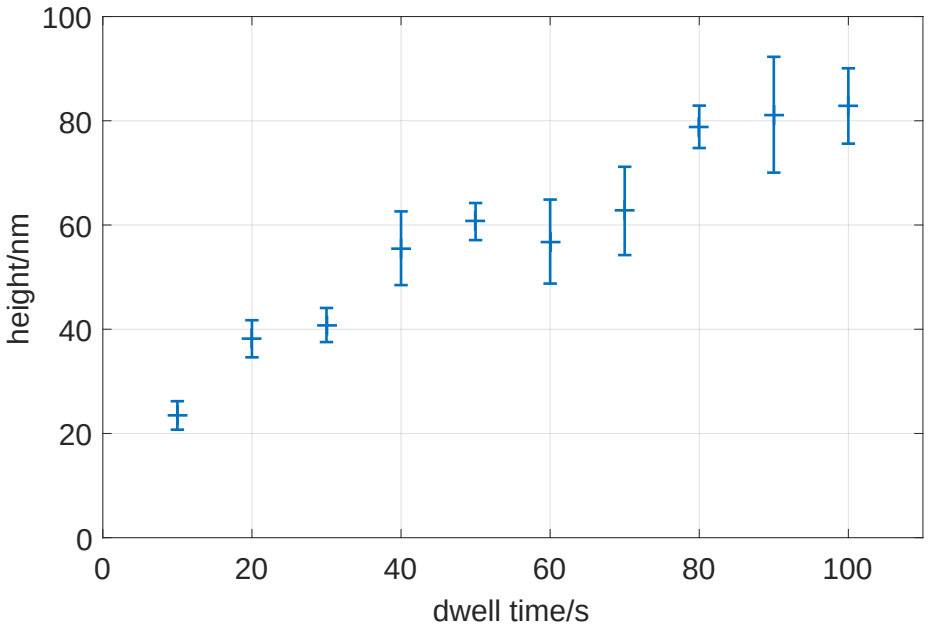

Figure 4.6: Dependence of height of the grown cones on dwell time for beam settings from Table 4.3. Substrate: TiO_2 c.

The dependence for Figure 4.6 is simple and exactly as could be expected. According to [17], for a surface diffusion driven reaction, the height should be proportional to t^a, where t is the dwell time. Table 4.4 shows the power a estimated for various beam settings.

Table 4.4: Calculated power a for various beam settings. The results suggest that the shape of the deposited material is similar for all studied settings and are in agreement with predictions and measurements in [17].

voltage/kV	current/pA	a (95 % confidence)
2	103	0,53 ± 0,11
2	12	0,42 ± 0,03
3	55	0,43 ± 0,16
5	64	0,46 ± 0,09
5	125	0,43 ± 0,15

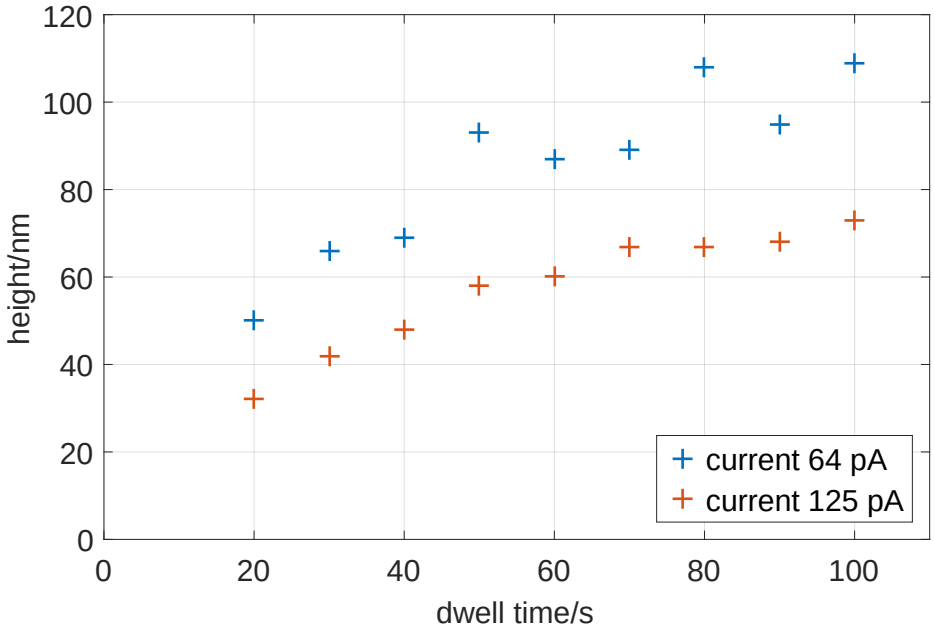

Figure 4.7: Height dependence on dwell time for accelerating voltage 5 kV. Substrate: TiO_2 c. Data were obtained by measuring with a little damaged AFM tip so there were many artifacts and obtaining reliable data was complicated. It is included for the sole purpose of demonstrating that the growth rates are similar for various voltages, errorbars are therefore omitted intentionally.

4.2.2. Height dependence on beam current

Figures 4.8 and 4.9 show heights of the cones for various beam intensities. This dependence came as a surprise. Based on [14], the dependence should be opposite from the one obtained by the experiments (supposing the deposited material is contamination).

Nevertheless, it gives a reason, why the growth is so substantial in FEG SEM Zeiss compared to LYRA3.

There are no measured data showing analogous dependencies for FEG SEM Zeiss. Since grids of dots were grown there, some limited information is available about the

height of the grown structures on a zirconia substrate. For 2 kV accelerating voltage and current 7 pA, the heights were approximately 120 nm for 5 s dwell time and 95 nm for 3 s dwell time. The rates are clearly much higher, which is probably caused by the beam current being so low. The vacuum chamber pressure was similar in both microscopes ($\approx 10^{-4}$ Pa).

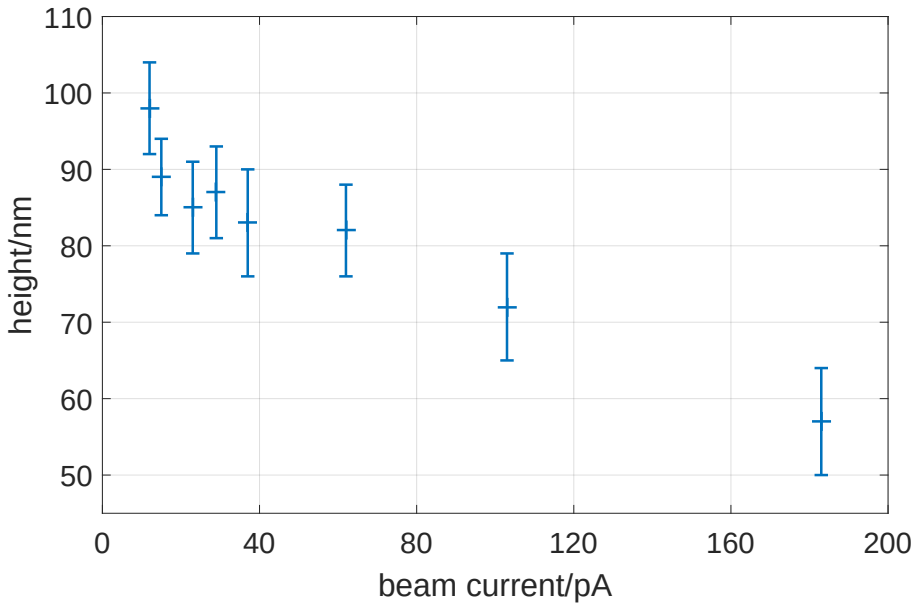

Figure 4.8: Height dependence on beam current for accelerating voltage 2 kV and dwell time 60 s. Substrate: TiO_2 c.

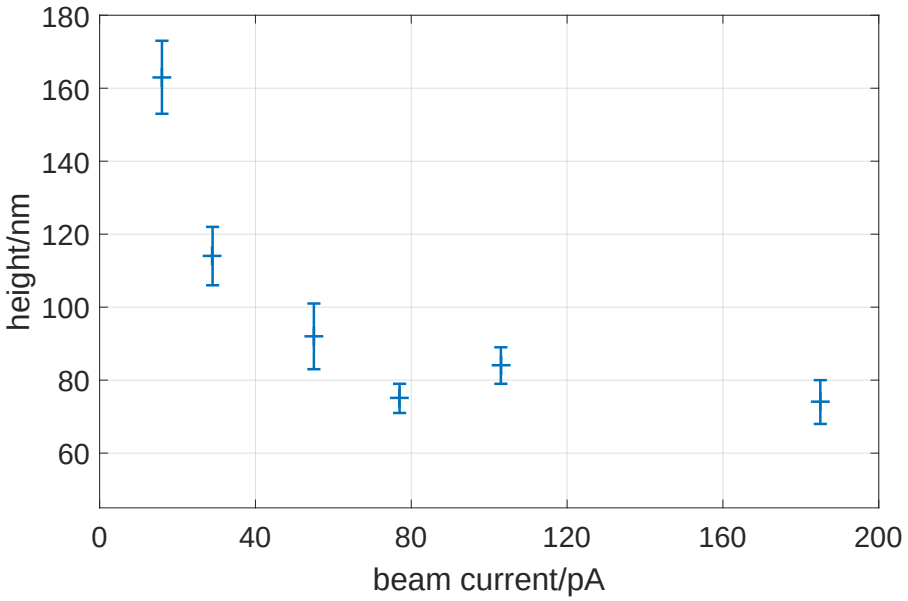

Figure 4.9: Height dependence on beam current for accelerating voltage 3 kV and dwell time 90 s. Substrate: TiO_2 c.

4.2.3. Width dependence on beam current and spot size

The width was measured as full width at half maximum and since some of the grown objects were very asymmetrical, the measurement was not very precise. Using Gwyddion, each width was measured 5 times and the standard error was determined from the differences in these measurements. It is interesting that for current higher than approximately 200 pA (and therefore bigger spot sizes, too), the profile of the structure changed from a single cone to a crown-like shape as can be seen in Figure 4.10. The cone width is in a relation with the beam spot size, but the deposited pillars are not very symmetrical so the data have large errors and determining the volumetric growth is therefore problematic.

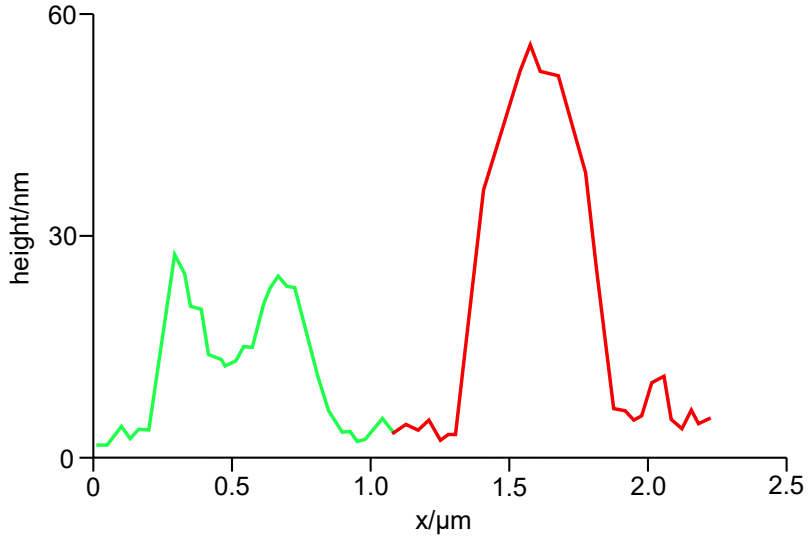

Figure 4.10: Comparison of the cross sections of the grown structures for left: 185 pA and right: 316 pA at 2 kV and dwell time 60 s. Substrate: TiO_2 c.

Table 4.5 shows the corresponding parameters and widths.

Table 4.5: Width dependence on current and spot size. Voltage 3 kV, dwell time 90 s. Substrate: TiO_2 d.

current/pA	spot size/nm	current density/A·cm^{-2}	width/nm
16	9,9	15	340 ± 20
29	8,4	37	350 ± 30
55	7,5	89	200 ± 20
77	7,7	118	260 ± 20
103	9,0	116	220 ± 30
185	16	66	310 ± 60

4.2.4. Influence of the accelerating voltage

The range of voltages for which the growth was studied was limited by the imaging quality and charging. In FEG SEM Zeiss, it is possible to use voltages below 1 kV, in LYRA3, however, the lower limit was 2 kV.

Widths and heights of the cones are compared in Table 4.6.

Table 4.6: Comparison of cone parameters for different accelerating voltages. The dwell time was 60 s and current 64 pA. Substrate: TiO_2 c.

voltage/kV	height/nm	width/nm
2	74 ± 4	190 ± 30
3	78 ± 3	170 ± 20
5	91 ± 5	200 ± 30

There were not enough experiments conducted to prove it, but from the data acquired, it looks as though the size is not significantly dependent on the accelerating voltage, though the values indicate a slight increase in height for 5 kV. It is nevertheless important to consider the charging effect at higher voltages. The induced electric field can cause the impacting electrons to be deflected from the intended spot.

4.2.5. Estimation of the volumetric growth rate

For beam current 12 pA, which proved to increase the growth, a series of structures were grown. Figures 4.11, 4.12 and 4.13 show their measured and calculated parameters.

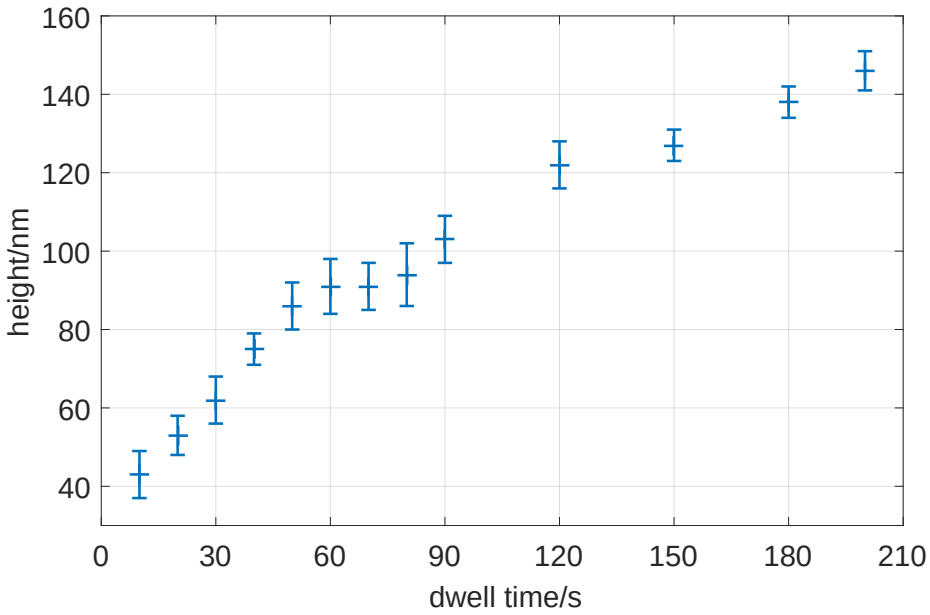

Figure 4.11: Dependence of heights of cones on dwell time for beam current 12 pA and accelerating voltage 2 kV, substrate TiO_2 c.

For simplicity's sake, the pillars were calculated with as if they were cones of volume V calculated according to

$$V = \frac{1}{3}\pi \cdot h \cdot \mathrm{FWHM}^2,$$

where h is the measured height and FWHM is the full width at half maximum.

The errors were calculated according to the rules for propagation of uncertainty and assuming zero correlation for simplicity.

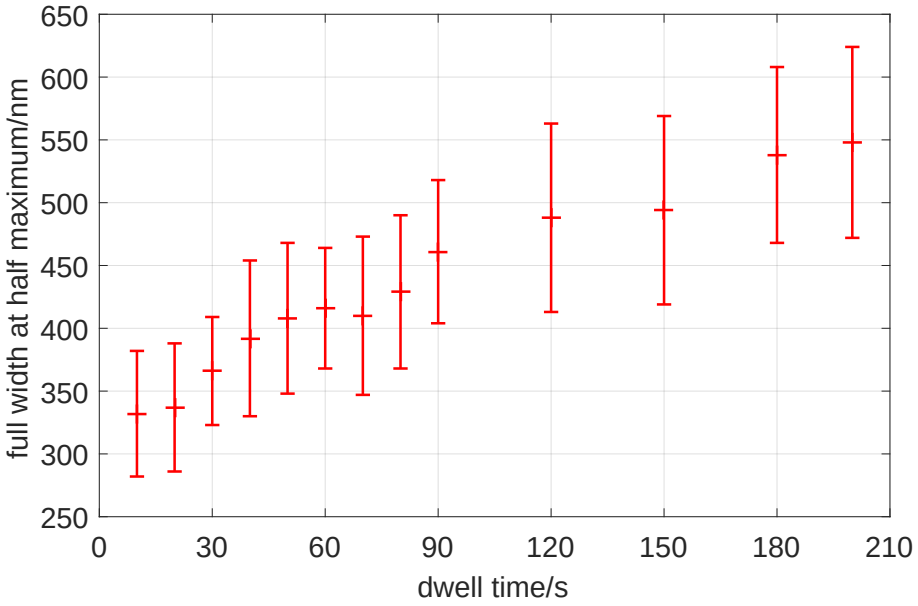

Figure 4.12: Dependence of full widths at half maximum (FWHM) of the cones on dwell time for beam current 12 pA and accelerating voltage 2 kV, substrate TiO_2 c.

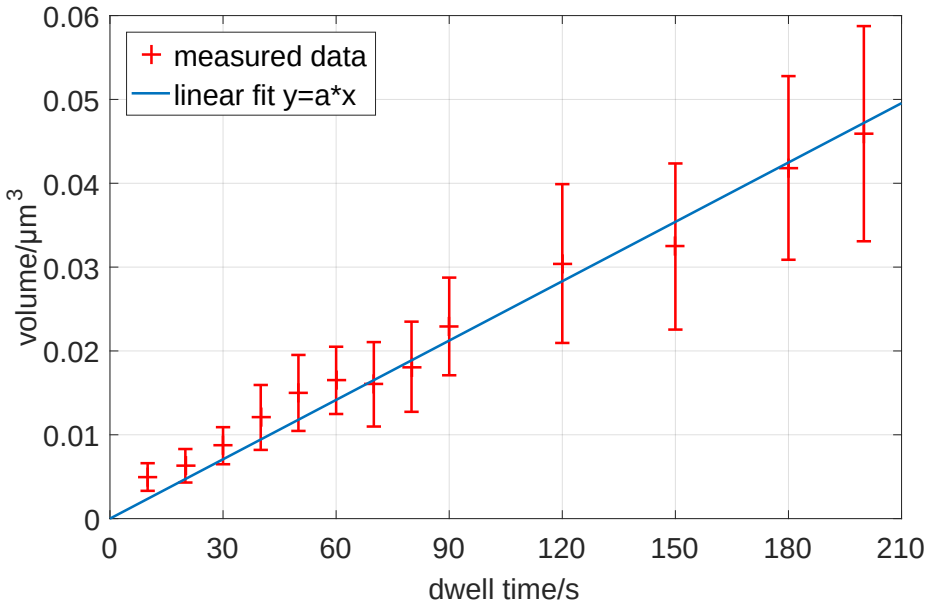

Figure 4.13: Estimation of the structures' volume dependence on dwell time for beam current 12 pA and accelerating voltage 2 kV, substrate TiO_2 c. The fit (using Gnuplot 5.0) provided a volumetric growth rate $(2{,}36{\cdot}10^{-4} \pm 0{,}06{\cdot}10^{-4})\ \mu m^3{\cdot}s^{-1}$.

4.3. Preliminary results of analysis by SIMS

Structures grown on the surface of zirconia were large enough to be analysed by secondary ion mass spectroscopy[3]. Figure 4.14 shows the analysed structure which was grown in FEG SEM Zeiss overnight at accelerating voltage 2 kV and current 8 pA. Charging caused some drift of the beam over time so the dwell times are unknown but the irradiation was sufficient to induce growth of a rather large structure. The analysis proved that the grown structures are composed of carbon and hydrocarbons as can be seen in Figure 4.15. The analysis was only superficial, since almost no mass from the structure was removed by the ion beam as shown in Figure 4.14. The borders of the irradiated area showed a stronger presence of more complex hydrocarbons, whereas the most extensively irradiated area seemed to be composed especially of carbon and shorter hydrocarbons.

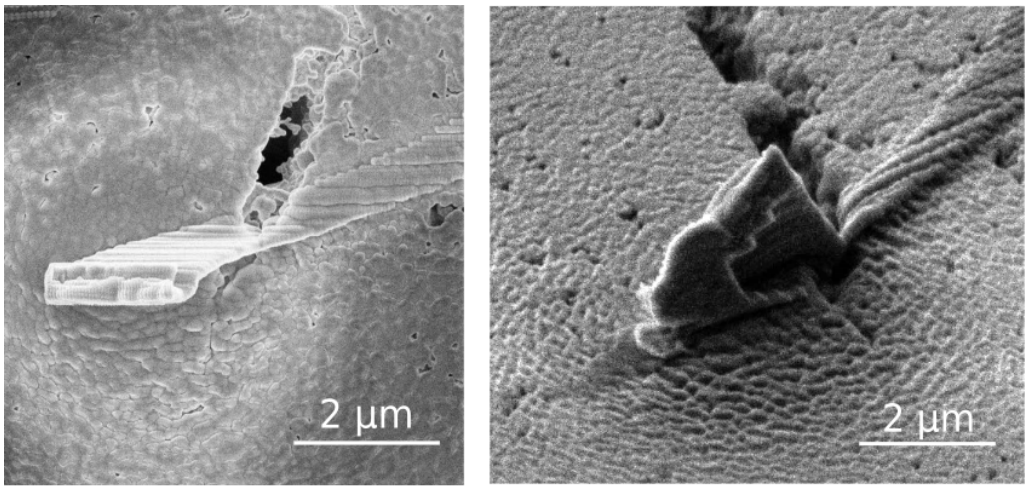

Figure 4.14: Left: The structure on zirconia substrate before the analysis by SIMS. Right: The structure grown on zirconia after the analysis by secondary ion mass spectroscopy, tilt of the sample was 55°. The structure was analysed only very superficially.

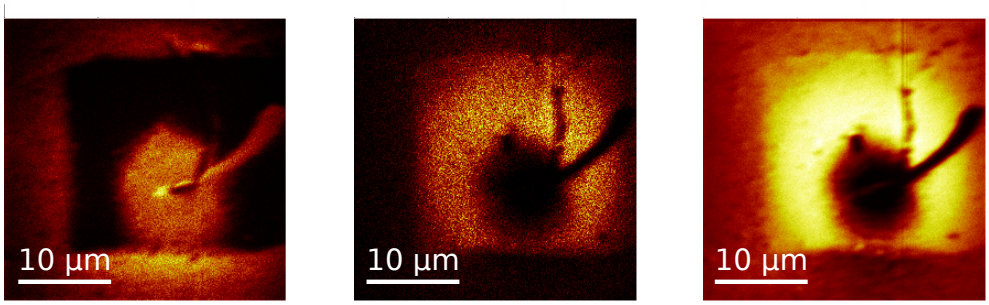

Figure 4.15: Relative signal strength of a) C b) ZrO_2 c) O at the surface of the modified zirconia.

The analysis was conducted only very recently and the results are not completely examined yet.

[3] A method used to analyse the composition of solid surfaces and thin layers. Focused primary ion beam causes cascade collisions and generated secondary ions are collected. It provides a three-dimensional analysis with little fragmentation [36].

5. Discussion

The main goal of this thesis was to describe the conditions which trigger the growth of structures on ceramic substrates.

Firstly, simulations of electron penetration and energy loss were meant to provide information about a possible localised heating. CASINO provided the energy absorbed by the sample and the output was modified to be compatible with COMSOL Multiphysics. Thermal effects calculated using the stationary model seem to be very reasonable and agree with observations and approximative calculations reported in literature [9]. The resulting temperature rise is in units or tens of °C for both materials so the possibility of the process being thermally driven can be dismissed. There is a certain level of negligence concerning describing the effect of individual electrons as continual heating but the proposed method could work very well for higher currents where the times between electrons are shorter than their relaxation times in material. Furthermore, a temperature rise in smaller samples heated by SEM or TEM operating as a stationary probe could be relatively easily estimated by a modification of the proposed method, especially since the large bulk approximations such as 2.5 no longer suffice for such cases. More advanced methods (presented in detail for example in [31]) must be used if a transport of mass or very low electron energies are to be considered.

A comparison between calculated temperature and an experiment was meant to verify the chosen method. Irradiating polylactic acid, which should undergo glass transition at temperatures 50−60 °C, started to have an effect for beam current 63 pA at 2 kV accelerating voltage. The result looked like a shrinkage, which is common for plastic materials [37], so it is hard to tell, if some of the damage could be caused thermally. Based on the calculation, the sample surface heated only by 5 °C.

The experimental part of the thesis focuses on finding conditions at which the growth of 3D structures is most extensive.

Initially, the growth was tested on rough samples or fractured ones, so it is possible the growth was often obscured. Direct application of polished ceramic samples did not originally seem possible since the growth was not observed on them. However, after thermal etching of the samples, the growth was activated. Roughening of the surface by revealing grain boundaries could be connected to the change. Only after conducting the experiments on flat polished surfaces, AFM analysis became an option and revealed a lot about the structures and their formation.

As it turns out, the original assumption that the growth rate is greater for higher current densities slowed the experiments a lot. Only after measuring the cones' height for different beam intensities using AFM, the real dependence was determined and adjusting the parameter ranges worked with made growing larger structures in SEM possible.

The height depends inversely on electron beam current. This dependence was observed for all measurements and explains why in FEG SEM Zeiss, the structures were always growing fast compared to Tescan LYRA3, in which the order of magnitude of current for standard imaging is higher. This result is in conformity with [15]. It might be accounted for by the following: the e-beam has both a constructive and a destructive effect on the hydrocarbon layers. The hydrocarbon deposition is limited by the diffusion of free neutral compounds towards the beam. If the current is too high, this source is slower than the deposition and the layer becomes more frequently re-ionised. The diffusion rate therefore limits the continuous contamination growth for high beam currents.

Structures' symmetry is limited by the perfection of beam focus and correction of astigmatism which, together with AFM artifacts, made measuring the width of structures less precise. For wider beams (bigger spot size, high current), the profile changed from a single peak to a crown-like shape. This effect is typically present as a result of a continuous irradiation of a larger area – the contamination layer is thicker at its edges in such cases.

An estimation of volumetric growth rate for beam current 12 pA and voltage 2 kV was calculated. The result was $(2{,}36{\cdot}10^{-4} \pm 0{,}06{\cdot}10^{-4})$ $\mu m^3{\cdot}s^{-1}$. Measured data suggest that the growth is continuous (even linear) during time.

Two possibilities were considered: the material needed for the structures growth comes from the sample or from the surrounding residual gas in the vacuum chamber. The latter has been observed quite commonly in the past [15, 16].

There were attempts to determine the exact composition of the manufactured structures by Auger electron spectroscopy, X-ray photoelectron spectroscopy and secondary ion mass spectroscopy (SIMS). Due to the excessive charging of the samples or other technical complications, only SIMS provided some data so far. According to the first surface analysis, the deposited material is mostly carbon and hydrocarbons. There are some differences of composition at the centre and edges of the irradiated area but this effect must be analysed further to make any conclusions. It could be very interesting to analyse the interface between the substrate and the contamination layers.

As to the origin of the hydrocarbons which are the precursor for the growth, there are two sources – sample surface and vacuum chamber residual gas. The experiments suggest that the surface diffusion is the main source of the material since the samples which show the increased growth rate have roughened surface due to the applied thermal etching and the contamination rate is not as high when irradiating other samples at the same conditions (for example gold coated wafers). The substrate has a big influence on whether the hydrocarbons form a continuously growing layers. No growth occurred on some of the samples, but further analysis must be conducted to determine the influence of sample history (e.g. thermal annealing, polishing) and the reason why some ceramic materials promote the contamination growth.

6. Conclusions

Conducted experiments specified conditions which cause the most apparent formation of 3D structures. The growth was tested for accelerating voltages 2−5 kV and beam currents 10^0−10^2 pA. Height of the grown structure can reach 100 nm in 60 s and surprisingly, the rate depends inversely on the beam current. There is most likely a specific beam current, below which the rate declines since the molecules get ionised less frequently. Due to technical limitations, the lowest beam current tested was 8 pA so the value for which the dependence changes was not found.

Volume of the deposited material increases linearly with time. A high volumetric growth rate estimated as $(2{,}36{\cdot}10^{-4} \pm 0{,}06{\cdot}10^{-4})$ $\mu m^3{\cdot}s^{-1}$ was measured on TiO_2 sample, beam current 12 pA and accelerating voltage 2 kV.

Since the growth is more apparent for lower beam currents, for which the temperature surely changes to a lesser extent, and the temperature rise calculation based on Monte Carlo simulations showed that the sample is locally heated by units or tens of K when the beam current is only pA, the process is presumably not thermally driven.

The material deposited was identified as hydrocarbon and carbon contamination by secondary ion mass spectroscopy. It most likely comes from the surface of the ceramic samples because the grain boundaries are grooved due to thermal etching and the growth is not present for all samples at the same rate. A specific reason why the contamination rate is so massive for certain samples, was not found.

The ability to manufacture relatively thick and large contamination layers gives us a chance to study the chemical composition by methods such as secondary ion mass spectroscopy. In the near future, analysis by HRTEM (high resolution transmission electron microscopy) will be conducted. Further analysis by SIMS is planned as well since it revealed a lot about the structures' composition already.

Bibliography

[1] RIEDEL, Ralf and I-Wei CHEN. *Ceramics science and technology. Vol. 2, Materials and properties*. Weinheim: Wiley-VCH, 2010, xxvi, 862 s. : il. ISBN 9783527311569.

[2] CARTER, C. Barry and M. Grant NORTON. *Ceramic materials: science and engineering*. 2nd ed. New York: Springer, 2013, xxxiii, 766 s. ISBN 9781461435228.

[3] NIEPCE, Jean-Claude, BOCH, Philippe, ed. Ceramic materials; processes, properties and applications. *Scitech Book News* [online]. Portland: Ringgold, 2007, **31**(2) [cit. 2017-04-11]. ISSN 01966006.

[4] PEREGO, Céline, Renaud REVEL, Olivier DURUPTHY, Sophie CASSAIGNON and Jean-Pierre JOLIVET. Thermal stability of TiO2-anatase: Impact of nanoparticles morphology on kinetic phase transformation. *Solid State Sciences* [online]. 1006, **12**(6), 989-995 [cit. 2017-01-30]. DOI: 10.1016/j.solidstatesciences.2009.07.021. ISSN 12932558 .

[5] KHATAEE, Alireza and G Ali MANSOORI. Nanostructured Titanium Dioxide Materials: Properties, Preparation and Applications. *ProtoView* [online]. Beaverton: Ringgold, 2014, **1**(19), 1-7 [cit. 2017-01-28].

[6] KERN, Philippe, Christian JAEGGI, Ivo UTKE, Vinzenz FRIEDLI and Johann MICHLER. Local electron beam induced reduction and crystallization of amorphous titania films. *Applied Physics Letters* [online]. 2006, **89**(2) [cit. 2017-01-28]. DOI: 10.1063/1.2219398. ISSN 00036951.

[7] REIMER, Ludwig. *Image formation in low-voltage scanning electron microscopy*. Bellingham, Wash: SPIE Optical Engineering Press, 1993, xii, 143 p. : ill. ;. ISBN 0819412066.

[8] EGERTON, Ray F. *Physical principles of electron microscopy: an introduction to TEM, SEM, and AEM*. New York: Springer, 2008, xii, 202 s. : il. ISBN 9780387258003.

[9] EGERTON, R.F., P. LI and M. MALAC. Radiation damage in the TEM and SEM. *Micron* [online]. Elsevier, 2004, **35**(6), 399-409 [cit. 2016-12-30]. DOI: 10.1016/j.micron.2004.02.003. ISSN 09684328.

[10] BELL, David C. and Natasha ERDMAN. Introduction to the Theory and Advantages of Low Voltage Electron Microscopy. *Low Voltage Electron Microscopy* [online]. Chichester, UK: John Wiley, 2012 [cit. 2016-12-30]. DOI: 10.1002/9781118498514.ch1. ISBN 9781118498514.

[11] FITTING, H.-J. Six laws of low-energy electron scattering in solids. *Journal of Electron Spectroscopy and Related Phenomena* [online]. Elsevier B.V, 2004, **136**(3), 265-272 [cit. 2016-12-31]. DOI: 10.1016/j.elspec.2004.04.003. ISSN 03682048.

[12] MATĚJKA, František. *Praktická elektronová litografie*. Brno: Ústav přístrojové techniky AV ČR, 2013. ISBN 9788087441046.

[13] JOY, David C. and Carolyn S. JOY. Low voltage scanning electron microscopy. *Micron* [online]. Elsevier, 1996, **27**(3), 247-263 [cit. 2017-03-05]. DOI: 10.1016/0968-4328(96)00023-6. ISSN 09684328.

[14] THONG, John T. L. *Electron beam testing technology*. New York: Plenum Press, c1993. ISBN 0306443600.

[15] HIRSCH, P., M. KÄSSENS, M. PÜTTMANN and L. REIMER. Contamination in a scanning electron microscope and the influence of specimen cooling. *Scanning* [online]. 1994, **16**(2), 101-110 [cit. 2017-02-19]. DOI: 10.1002/sca.4950160207. ISSN 01610457.

[16] UTKE, Ivo, Stanislav MOSHKALEV and Phillip RUSSELL. *Nanofabrication using focused ion and electron beams: principles and applications*. Oxford: Oxford University Press, 2012, xvi, 813 s : il. ISBN 9780199734214.

[17] RYKACZEWSKI, Konrad, William B. WHITE and Andrei G. FEDOROV. 2007. Analysis of electron beam induced deposition (EBID) of residual hydrocarbons in electron microscopy. *Journal of Applied Physics* [online]. American Institute of Physics, **101**(5).

[18] POSTEK, Michael T., András E. VLADÁR and Kavuri P. PURUSHOTHAM. 1405. Does your SEM really tell the truth? How would you know? Part 2. *Scanning* [online]. **36**(3), 347-355.

[19] CHEE, See Wee, Shankar SIVARAMAKRISHNAN, Renu SHARMA and Jian-Min ZUO. Electron-Beam-Induced Growth of TiO 2 Nanostructures. *Microscopy and Microanalysis* [online]. Cambridge University Press, 2011, **17**(2), 274-278 [cit. 2016-12-30]. DOI: 10.1017/S1431927610094420. ISSN 14319276.

[20] HENDERSON, Michael A. Mechanism for the bulk-assisted reoxidation of ion sputtered TiO 2 surfaces: diffusion of oxygen to the surface or titanium to the bulk? *Surface Science* [online]. Elsevier B.V, 1995, **343**(1), L1156-L1160 [cit. 2017-01-30]. DOI: 10.1016/0039-6028(95)00849-7. ISSN 00396028.

[21] WANG, Li-Qiong, D.R. BAER and M.H. ENGELHARD. Creation of variable concentrations of defects on TiO 2(110) using low-density electron beams. *Surface Science* [online]. Elsevier B.V, 1994, **320**(3), 295-306 [cit. 2017-01-28]. DOI: 10.1016/0039-6028(94)90317-4. ISSN 00396028.

[22] SIMPSON, W.C., W.K. WANG, J.A. YARMOFF and T.M. ORLANDO. 1999. Photon- and electron-stimulated desorption of O+ from zirconia. *Surface Science* [online]. **423**(2-3), 225-231. Available at: http://linkinghub.elsevier.com/retrieve/pii/S003960289800908X

[23] IVIN, V.V, M.V SILAKOV, G.A BABUSHKIN, B LU, P.J MANGAT, K.J NORDQUIST and D.J RESNICK. Modeling and simulation issues in Monte Carlo calculation of electron interaction with solid targets. *Microelectronic Engineering* [online]. Elsevier B.V, 2003, **69**(2), 594-605 [cit. 2016-12-30]. DOI: 10.1016/S0167-9317(03)00351-4. ISSN 01679317.

[24] BINNIG, G., C. F. QUATE a Ch. GERBER. Atomic Force Microscope. *Physical Review Letters* [online]. 8603, **56**(9), 930-933 [cit. 2017-04-17]. DOI: 10.1103/PhysRevLett.56.930. ISSN 00319007.

[25] EATON, Peter Jonathan. a Paul. WEST, 2010. *Atomic force microscopy*. New York: Oxford University Press. ISBN 9780199570454.

[26] DROUIN, Dominique, Alexandre Réal COUTURE, Dany JOLY, Xavier TASTET, Vincent AIMEZ and Raynald GAUVIN. CASINO V2.42 – A Fast and Easy-to-use Modeling Tool for Scanning Electron Microscopy and Microanalysis Users. *Scanning* [online]. San Francisco: Wiley Subscription Services, Inc., A Wiley Company, 0705, **29**(3), 92-101 [cit. 2017-02-26]. DOI: 10.1002/sca.20000. ISSN 01610457.

[27] *MatWeb: Online Materials Information Resource* [online], [cit. 2017-04-17]. Available at: http://www.matweb.com

[28] *NIST WebBook Chemie* [online], [cit. 2017-04-17]. Available at: http://webbook.nist.gov

[29] *Emissivity of Common Materials* [online], Norwalk [cit. 2017-04-29]. Available at: https://www.omega.com/literature/transactions/volume1/emissivityb.html

[30] HUEBENER,R.P., Scanning Electron Microscopy at Very Low Temperatures, *Advances in Electronics and Electron Physics* [online], Volume 70, 1988, Pages 1-78[cit. 2017-04-22]. DOI: 10.1016/S0065-2539(08)60339-X. ISSN 0065-2539.

[31] BASIL T. WONG and PINAR M. MENGÜÇ. *Thermal transport for applications in nanomachining*. Berlin: Springer, 2007. ISBN 9783540736073.

[32] GUILLON, Olivier, Jesus GONZALEZ-JULIAN, Benjamin DARGATZ, Tobias KESSEL, Gabi SCHIERNING, Jan RÄTHEL and Mathias HERRMANN. 2014. Field-Assisted Sintering Technology/Spark Plasma Sintering: Mechanisms, Materials, and Technology Developments. *Advanced Engineering Materials*. **16**(7), 830-849.

[33] DrawBeam Software, *TESCAN* [online]. Brno [cit. 2017-04-29]. Available at: http://www.tescan.com/en-us/technology/accessories/drawbeam-software

[34] NANOSENSORS Akiyama-Probe, *NANOSENSORS Website* [online]. Neuchâtel [cit. 2017-04-22]. Available at: http://www.akiyamaprobe.com/specs/specifications-of-a-probe/

[35] *Polylactid Acid - MakeItFrom.com* [online], [cit. 2017-04-29]. Available at: http://www.makeitfrom.com/material-properties/Polylactic-Acid-PLA-Polylactide/

[36] Secondary Ion Mass Spectroscopy ION-TOF TOF.SIMS5, *CEITEC* [online]. Brno [cit. 2017-04-30]. Available at: https://www.ceitec.cz/secondary-ion-mass-spectroscopy-ion-tof-tof-sims5/e471?researchGroup=90

[37] FRANK, Joachim, ed., c2006. *Electron tomography: methods for three-dimensional visualization of structures in the cell*. 2nd ed. New York: Springer. ISBN 9781441921727.

List of abbreviations

3Y-TZP	3 molar percent yttria stabilized tetragonal zirconia polycrystal
AFM	Atomic force microscope
Al_2O_3	Aluminium oxide or alumina
BSE	Backscattered electrons
CaO	Calcium peroxide
CIP	Cold isostatic pressing
CSDA	Continuous slow down approximation
DC	Direct current
DCS	Differential cross section
EBL	Electron beam lithography
FIB	Focused ion beam
HRTEM	High resolution transmission electron microscope
LaB_6	Lanthanum hexaboride
MgO	Magnesium oxide
PLA	Polylactic acid
SE	Secondary electrons
SEM	Scanning electron microscope
SIMS	Secondary ion mass spectroscopy
SPS	Spark plasma sintering
STE	Surface transport equation
TEM	Transmission electron microscope
TiO_2	Titanium dioxide or titania
XPS	X-ray photoelectron spectroscopy
Y_2O_3	Yttrium(III) oxide or yttria
ZrO_2	Zirconium dioxide or zirconia